Redirection of SARS-CoV-2 to Phagocytes by Intranasal sACE2-Fc as a Universal Decoy Confers Complete Prophylactic Protection

Jingyi Wang[a]†, Jiangchuan Li[a]†, Alex W. Chin[b,c]†, Bin Luo[a,d], Junkang Wei[a], Jiale Qiu[a], Jianwei Ren[a,d], Yin Xia[a], Thomas Braun[a,e], Leo L.M. Poon[b,c,f]*, Bo Feng[a,d,g]*

[a] School of Biomedical Sciences, Faculty of Medicine; GIBH CAS-CUHK Joint Research Laboratory on Stem Cell and Regenerative Medicine, The Chinese University of Hong Kong; Hong Kong SAR, China.

[b] School of Public Health, LKS Faculty of Medicine, The University of Hong Kong; Hong Kong SAR, China.

[c] Centre for Immunology & Infection, Hong Kong Science and Technology Park; Hong Kong SAR, China.

[d] Centre for Regenerative Medicine and Health, Hong Kong Institute of Science & Innovation, Chinese Academy of Sciences; Hong Kong SAR, China.

[e] Department of Cardiac Development and Remodeling, Max-Planck-Institute for Heart and Lung Research, 61231, Bad Nauheim, Germany.

[f] HKU-Pasteur Research Pole, LKS Faculty of Medicine, The University of Hong Kong; Hong Kong SAR, China.

[g] Guangzhou Institutes of Biomedicine and Health, Chinese Academy of Sciences; Guangzhou 510530, China.

* Corresponding authors. Email: llmpoon@hku.hk (L.L.P.); fengbo@cuhk.edu.hk (B.F.).

† These authors contribute equally.

ABSTRACT

The rapid evolution of SARS-CoV-2 and other respiratory RNA viruses limits the success of current vaccines and antibody-based therapies. Engineered decoy receptors based on soluble angiotensin-converting enzyme 2 (sACE2) offer promising alternatives. Clinical-grade recombinant sACE2 inhibits SARS-CoV-2 replication *in vitro* but shows limited clinical success. This study reports an optimized sACE2 mutant fused to human IgG1 Fc (B5-D3), which redirects virus–decoy complexes to lysosomal degradation in macrophages. Intranasal prophylactic delivery of B5-D3 confers complete protection in SARS-CoV-2-infected K18-hACE2 mice. Abrogation of Fc effector functions compromises antiviral protection, indicating that Fc-mediated uptake of virus–decoy complexes is critical. Transcriptomic analysis suggests that B5-D3 induces early immune activation in lungs of infected mice. Bio-distribution and flow cytometry reveal selective targeting of airway phagocytes. *In vitro* assays confirm lysosomal degradation of virus–decoy complexes by macrophages without productive infection. These findings reveal a distinct antiviral mechanism via phagocytic clearance, supporting refined regimens for decoy treatments against SARS-CoV-2 and potentially other respiratory viruses.

KEYWORDS

sACE2-Fc, SARS-CoV-2, intranasal prophylaxis, Fc-mediated effector function, phagocytosis, decoy receptor

INTRODUCTION

The incessant evolution of severe acute respiratory syndrome coronavirus 2 (SARS-CoV-2) and frequent breakthrough infections during the coronavirus disease 2019 (COVID-19) pandemic underscore the critical need for effective antiviral strategies that are less susceptible to immune escape than conventional vaccines and monoclonal antibody (mAb) therapies [1].

Soluble angiotensin-converting enzyme 2 (sACE2) therapies, which employ recombinant forms of the human angiotensin-converting enzyme 2 (ACE2) receptor—the primary binding site for the SARS-CoV-2 spike protein [1-5]—as viral decoys, have emerged as a promising alternative [6]. However, an early clinical version (amino acid [aa] 1-740, APN01) showed limited therapeutic benefit [7] and raised safety concerns about interference with endogenous renin-angiotensin system (RAS) [8]. Subsequent protein engineering greatly improved the pharmacological properties of sACE2, including fusion with a human IgG1 Fc domain (sACE2-Fc) to enhance serum half-life [9], and mutagenesis to enhance spike-binding affinity [10-12] and abolish enzymatic activity [10, 12, 13]. Potent sACE2-Fc mutants have shown broad-spectrum neutralization against SARS-CoV-2 variants in animal models [14-16]. However, their efficacy in protecting hosts from viral infections was often incomplete. Despite the evidence suggesting a role for Fc-mediated effector functions in sACE2-Fc efficacies [14], underlying immune mechanisms remained poorly understood. Further investigation that systematically assesses the potential to optimize decoy design, strategies of administration, and mechanisms of actions is pivotal to the development of ACE2 decoy-based antivirals and harnessing their full potential.

In this study, we engineered a potent yet minimally mutated sACE2-Fc decoy candidate (B5-D3) with just two mutations to enhance spike-binding (T92Q) while eliminating enzymatic activity (H374N). Broad-spectrum neutralization capacity against multiple SARS-CoV-2 variants was

67 confirmed by *in vitro* neutralization assays. Markedly, stepwise examinations of various
68 administration routes and time points identified intranasal (IN) prophylaxis as the most effective
69 regimen for B5-D3, which conferred complete protection against SARS-CoV-2 infection in K18-
70 hACE2 mice across age groups. Whereas B5-D3 intravenously administered either prior or post
71 infection, showed activity that moderately improved disease outcome. To understand how sACE2-
72 Fc decoys influence viral fate and achieve superior antiviral protection via IN prophylaxis, we
73 carried out systematic, mechanistic investigations through transcriptomics, bio-distribution, and
74 phagocytosis analysis. Our results revealed that IN-delivered B5-D3 engages airway phagocytes to
75 promote early viral clearance and host immune activation, which uncovers a distinct antiviral
76 mechanism and offers a universal and commonly applicable "decoy strategy" to combat unknown
77 air-borne respiratory virus in the future.

78

79 **RESULTS**

80 **Engineered sACE2-Fc decoys with two single mutations achieve robust neutralization against**
81 **SARS-CoV-2 variants**

82 To generate representative ACE2 decoys with optimal performance, we adopted the established
83 sACE2-Fc fusion design [9] (Fig. 1a; Supplementary Fig. 1) and selectively verified mutation(s)
84 proposed in prior studies, either to enhance the binding of human ACE2 to SARS-CoV-2 spikes [17]
85 (B2–B6) or to abolish enzymatic activity [10-12, 18] (A2, A3, D1–D5) (Supplementary Fig. 2a,b).
86 The sACE2-Fc candidates generated with either type of mutation(s) were all verified for
87 pseudovirus-based neutralization assays [19] and ACE2 enzymatic activity. Indeed, mutants B2–B6
88 showed consistently enhanced neutralization capacity against both Wuhan-Hu-1 and D614G
89 pseudoviruses [20] (Fig. 1b; Supplementary Fig. 2c,d). Notably, B5 with the single T92Q mutation,

which increases spike affinity by removing a critical glycosylation site at N90 [21], exhibited remarkable neutralization enhancement among other multi-mutants. Meanwhile, mutations selected for catalytic inactivation, including the previously reported mutation pairs A2 [11, 18], A3 [10], single mutations derived from these pairs (D1, D3, D4, but not D2), and a recently reported single mutation D5 [12], effectively abolished enzymatic activity while showing minimal effect on spike binding (Fig. 1b; Supplementary Fig. 2e). We next combined the B5 (T92Q) mutation with each of the inactivating mutations. Notably, among the resulting compound mutants, B5-D1, B5-D3, B5-D4, and B5-D5 with two mutations remained to be enzymatically inactive while retaining comparable or stronger neutralization capacity than B5-A2 and B5-A3 with three mutations (Fig. 1b; Supplementary Fig. 2f–h). B5-D3 (T92Q/H374N) emerged as one of the best candidates (Fig. 1a, red stars; Fig. 1b, red arrow), exhibiting minimal deviation from wild type (WT) ACE2 in structural modeling (root mean square deviation [RMSD] = 0.212 Å; Supplementary Fig. 2i) [22].

To assess the breadth of neutralization, we tested three double mutants (B5-D3, B5-D4, and B5-D5) against pseudoviruses bearing spikes from various variants of concern (VOCs) and variants of interest (VOIs) [1, 23-27]. All three designs showed dose-dependent neutralization with higher potency than WT sACE2-Fc (Fig. 1c,d; Supplementary Fig. 3). We further examined B5-D3, as a representative decoy candidate, against authentic SARS-CoV-2 using plaque reduction neutralization tests (PRNTs) in Vero E6 cells, which indeed, confirmed its robust activity against Wuhan-Hu-1, Delta, and Omicron variants BA.5, BQ.1.22, and XBB.1.5 strains [1, 24, 28, 29] (Fig. 1e-g). In contrast, Casirivimab, serving as positive control [30], showed efficacy only against early variants (Wuhan-Hu-1 and Delta; Fig. 1f), but failed to neutralize Omicron sublineages (Fig. 1g). These results demonstrate that a rationally engineered sACE2-Fc decoy with only two mutations could achieve potent and safe neutralization across SARS-CoV-2 variants, reducing the potential risks associated with extensive mutagenesis.

114

115 **Prolonged *in vivo* overexpression of sACE2-Fc double mutants demonstrates minimal RAS**
116 **disturbance and no tissue damage in mice**

117 Next, we evaluated the safety of the sACE2-Fc double mutants *in vivo* (Supplementary Fig. 4a).
118 Adult K18-hACE2 transgenic mice with immune tolerance to human ACE2 [31] were intravenously
119 injected with adenovirus-associated virus (AAV) vectors encoding either WT sACE2-Fc or double
120 mutants at a dose of 1×10^{11} genome copies (GC) per mouse. Notably, serum levels of the double
121 mutants (B5-D3, B5-D4, and B5-D5) were significantly higher than those of WT sACE2-Fc
122 (Supplementary Fig. 4b; Supplementary Table 1). This trend was further supported by quantification
123 of AAV genomes in the liver, indicating greater *in vivo* stability or tolerance of the double mutants
124 (Supplementary Fig. 4c).

125 Importantly, despite prolonged high-level expression, ELISA measurements of serum renin,
126 Angiotensin II (Ang II), and Ang (1–7) [8] demonstrated minimal disturbance to the RAS in mice
127 treated with the double mutants (Supplementary Fig. 4d–f). In contrast, WT sACE2-Fc treatment
128 led to significantly elevated serum levels of renin and Ang II, indicating a disruption of the RAS
129 (Supplementary Fig. 4d,e). Histological examination of multiple organs at the end point showed no
130 evidence of tissue damage in any of these groups (Supplementary Fig. 4g). These observations
131 collectively underscore the improved safety of catalytically inactive sACE2-Fc mutants, supporting
132 their suitability for prolonged or repeated use.

133

134 **Prophylactic administration of the sACE2-Fc B5-D3 mutant via the intranasal route exhibits**
135 **superior protection against SARS-CoV-2**

136 Next, we evaluated the *in vivo* efficacy of the sACE2-Fc double mutant B5-D3 against SARS-CoV-
137 2 infection using aged K18-hACE2 mice (10 – 12 months old) (Fig. 2a). 6 hours (h) before
138 inoculating with 1×10^4 plaque-forming unit (PFU) of SARS-CoV-2 (Wuhan-Hu-1 strain), mice
139 received a prophylactic dose of recombinant B5-D3 protein either intranasally (IN, 2.5 mg/kg) or
140 intravenously (IV, 15 mg/kg). To simulate a therapeutic intervention, an additional group received
141 IV B5-D3 (15 mg/kg) 24 h post-virus inoculation. The vehicle control group received an intranasal
142 PBS administration 6 h before viral challenge. Over a 14-day observation period, all mice in the
143 PBS group exhibited significant weight loss and succumbed to infection by 7 days post-infection
144 (dpi) (Fig. 2b,c, black lines). Both IV-treated groups exhibited initial weight loss similar to the PBS
145 group; however, two out of four mice in each group began to regain weight from 10 dpi and survived
146 until the observation endpoint, suggesting improvement in disease severity and survival (green and
147 blue lines). Notably, all mice in the IN-prophylaxis group, despite receiving a 6-fold lower dose of
148 B5-D3 protein than those in the IV groups, maintained stable body weight and achieved complete
149 survival over the 14-day period (red lines).

150 To monitor viral burden, one mouse from each group was sacrificed at 4 dpi (Fig. 2a). Corroborating
151 the body weight and survival data, no infectious viral particles were detected in lung homogenate
152 from the IN-prophylaxis mouse. In contrast, mice treated with IV prophylaxis or therapy showed
153 reduced but still detectable viral titers compared to the PBS group (Fig. 2d). Immunohistochemistry
154 (IHC) staining further confirmed the absence of viral nucleocapsid (N) protein in the IN-treated
155 mouse, whereas IV-treated mice showed residual infection and immune cell infiltration. H&E
156 staining revealed varying degrees of alveolar thickening in all SARS-CoV-2-inoculated mice (Fig.
157 2e).

158 To further explore the effective timing of IN administration that offers superior antiviral protection,

159 we treated a younger cohort of K18-hACE2 mice (2 – 3 months old) with B5-D3 (IN, 2.5 mg/kg) at
160 –24 h, –6 h, or +24 h relative to viral challenge (Fig. 2f). Consistently, all mice in the PBS group of
161 the young cohort exhibited substantial weight reduction from 4 dpi and reached approximately 20%
162 loss by 7 dpi (Fig. 2g, black lines). Whereas differently from the aged cohort, two of the five infected
163 young mice eventually recovered, resulting in 40% survival (Fig. 2g,h, black lines) indicating age-
164 related fitness [32]. Interestingly, both the –24 h and –6 h IN-prophylaxis groups maintained stable
165 body weights (Fig. 2g, pink and red lines), ending up with survival rates of 80% and 100%,
166 respectively (Fig. 2h). In contrast, the +24 h IN-therapy group showed substantial weight loss and
167 no survival improvement compared to the PBS group, indicating that high-efficiency antiviral
168 protection of IN B5-D3 is limited to prophylactic administration but not post-infection treatments
169 (Fig. 2g,h, orange lines). Consistently, virus-neutralizing antibodies were detected in surviving mice
170 from the PBS and +24 h groups at 14 dpi, indicating once active infection and subsequent immune
171 response. Whereas antibody levels remained minimal in the two IN-prophylaxis groups, suggesting
172 effective prevention of viral replication (Fig. 2i).

173

174 **Efficient protection against SARS-CoV-2 by intranasal B5-D3 prophylaxis depends on Fc-**
175 **mediated effector functions**

176 Adding on to the 2-week observation of the significant protection conferred by IN prophylaxis with
177 B5-D3, we examined the early responses following SARS-CoV-2 challenge in K18-hACE2 mice. A
178 new cohort of 2- to 3-month-old mice received B5-D3 IN treatment 6 h before infection (–6 h), and
179 lung tissues were harvested at 1, 2, and 4 dpi for analysis (Fig. 3a). An additional group was treated
180 with a modified version of B5-D3, which contains L234A/L235A mutations in the human IgG1 Fc
181 region (B5-D3-LALA) to abolish its binding to Fc gamma receptor (FcγR) and abrogate Fc effector

182 functions [33] (Supplementary Fig. 5). Quantitative PCR of viral spike (*S*) and nucleocapsid (*N*)
183 RNA in lung tissues revealed only marginal viral loads in the B5-D3-treated mice at as early as 1
184 dpi, indicating efficient suppression of early viral replication compared to the PBS group (Fig. 3b).
185 Analysis of infectious viral particles in lung homogenates further corroborated these observations,
186 demonstrating minimal or undetectable viral titers in the B5-D3 group at all time points (Fig. 3c).
187 In contrast, PBS-treated mice exhibited consistently high viral loads. Interestingly, the analysis of
188 B5-D3-LALA group detected varied levels of *S* and *N* RNAs and significant viral burdens in two
189 out of three mice, indicating partial protection and supporting that Fc effector functions are
190 indispensable for full efficacy of IN B5-D3 (Fig. 3b,c, right panels). Consistently, IHC staining for
191 N protein in lung sections confirmed the absence of viral infection in the B5-D3 groups at all time
192 points. Whereas signs of viral replication were evident in the lungs of mice treated with PBS since
193 as early as 1 dpi and in the B5-D3-LALA-treated cohort as examined at 4 dpi (Fig. 3d;
194 Supplementary Fig. 6, left panels). Despite variations in viral burden, H&E staining indicated
195 alveolar septal thickening in all groups (Fig. 3e; Supplementary Fig. 6, right panels; Supplementary
196 Fig. 7). Notably, moderate alveolar thickening persisted in the B5-D3-treated mice till the end point
197 at 4 dpi, whereas the PBS groups developed much severer alveolar thickening at 4 dpi. Consistent
198 with the partial protection observed with B5-D3-LALA, histological analysis of lung samples in this
199 group revealed severer yet heterogenous alveolar thickening (Supplementary Fig. 7). These findings
200 collectively demonstrated that IN prophylaxis with B5-D3 blocks SARS-CoV-2 infection not only
201 by neutralization but also by immune mechanisms such as Fc-mediated effector functions.

202

203 **RNA-Seq analysis of lung transcriptomes reveals early antigen presentation and prompt viral**
204 **clearance following SARS-CoV-2 neutralization by B5-D3**

205 To delineate the immune mechanisms underlying IN B5-D3-mediated prophylactic protection
206 against SARS-CoV-2, we examined the transcriptomes of lung samples collected at 1, 2, and 4 dpi
207 from the above experiment (Fig. 4a–d; Supplementary Fig. 8a). Unsupervised clustering based on
208 Pearson correlation distinguished samples with severe infection (mainly PBS-treated) from those
209 with subtle or no infection (mocks and most decoy-treated mice) (Supplementary Fig. 8a).
210 Corroborating the levels of viral infections observed, differential gene expression (DGE) analysis
211 revealed extensive inflammatory responses in the PBS groups, significantly greater than in mock
212 treatments. At 1, 2, and 4 dpi, 26, 1232, and 1756 genes were upregulated, respectively, and were
213 significantly enriched in Gene Ontology Biological Process (GOBP) terms related to antiviral
214 responses such as type I interferon (IFN) responses and innate immune responses (Fig. 4a,b;
215 Supplementary Fig. 8b–d) [34]. In stark contrast, DGE analysis between B5-D3 prophylaxis and
216 mocks at 1, 2, and 4 dpi showed subtle changes, with only 1, 7, and 32 genes upregulated,
217 respectively, and only moderate enrichment in chemotaxis-related pathways at 4 dpi (Fig. 4c;
218 Supplementary Fig. 8e). The B5-D3-LALA group, however, had 264 genes upregulated at 4 dpi
219 compared to the mocks, suggesting incomplete protection and ongoing viral activity (Fig. 4d;
220 Supplementary Fig. 8f).

221 To capture the immune activations specifically linked to B5-D3-triggered antiviral efficacy other
222 than infection-induced inflammation, we directly compared the B5-D3 and PBS groups (Fig. 4e-j;
223 Supplementary Fig. 9 and 10). Interestingly, at 1 dpi, the B5-D3 group exhibited enhanced
224 expression of several immune-related genes, including *Lef1* [35], *Fscn1* [36], *Kcne4* [37], *Tcrb*, and
225 *Ccl22* [38, 39], which are associated with early dendritic cell function and T cell activation (Fig. 4e).
226 Gene Set Enrichment Analysis (GSEA) of GOBPs and Kyoto Encyclopedia of Genes and Genomes
227 (KEGG) pathways further supported these findings (Fig. 4f,g). Chemotaxis and pathways related to
228 antigen presentation such as Rap1 signaling pathway [40] and Th1 and Th2 cell differentiation were

229 significantly activated in the B5-D3 group at 1 dpi compared to PBS group (Fig. 4h-j;
230 Supplementary Fig. 9a–c). Moreover, the B5-D3 groups showed enhancement in cilium movement
231 and metabolism of xenobiotics at both 2 and 4 dpi, suggesting active clearance of viral particles due
232 to effective early responses (Supplementary Fig. 10c–f).

233 Furthermore, we collectively examined the GOBPs that were significantly activated in B5-D3
234 groups at either 1, 2, or 4 dpi among all treatment groups and time points. Markedly, B5-D3 group
235 showed higher normalized enrichment scores (NES) in chemotaxis-related GOBP pathways than
236 PBS group at 1 dpi (Fig. 4k, purple boxes), while direct comparison between B5-D3 and PBS groups
237 further revealed the broad involvement of multiple types of effector immune cells (Fig. 4l, purple
238 box). These results collectively indicate that early immune activation is a hallmark of B5-D3-
239 mediated protection.

240 Finally, the lung transcriptomes from mice receiving B5-D3 without viral inoculation showed high
241 similarity to the PBS vehicle controls (Supplementary Fig. 11a). The 10 upregulated genes identified
242 showed poor correlation with the virus-inoculated B5-D3 group (Supplementary Fig. 11b,c),
243 supporting that early immune responses observed in B5-D3 IN prophylaxis groups were primarily
244 triggered by virus neutralization rather than by B5-D3 alone.

245

246 **Intranasally delivered B5-D3 is enriched in the respiratory tract and targets mainly the airway**
247 **macrophages**

248 The superior prophylactic antiviral effects of IN over IV administration of B5-D3 as observed in the
249 K18-hACE2 infection experiments (Fig. 2a–e) suggested the importance of mobilizing the local
250 immunity within the respiratory tract. Next, we labeled B5-D3 protein with Alexa Fluor 750 (AF750)
251 and examined its bio-distribution and kinetics after IN administration (Fig. 5a). *In vivo* imaging

252 showed that fluorescence-labeled B5-D3 (B5-D3-AF750) was present in the nasal cavities for at
253 least 24 h after a single IN dose in K18-hACE2 mice (Fig. 5b). *Ex vivo* images further revealed that
254 B5-D3-AF750 distributed in the respiratory tract from nasal cavity to lung within 20 min and
255 remained enriched in lungs by 24 h after administration (Fig. 5c). In contrast, non-respiratory organs
256 showed minimal signals, which were merely detectable in urinary system and liver (Fig. 5d).

257 To identify the immune cells in the respiratory tract that are actively engaged with IN B5-D3, we
258 performed flow cytometry analysis on bronchoalveolar lavage fluid (BALF) at 6 h after IN
259 administration of B5-D3-AF750 (Fig. 5e). Like normal conditions, over 95% of live BALF cells
260 were $CD45^+$ immune cells, predominantly composed of $CD11c^+$Siglec-F^+ resident alveolar
261 macrophages (AMs) (> 50%) in both treatment and vehicle groups (Fig. 5f; Supplementary Fig. 12).
262 Notably, the IN administered B5-D3-AF750 was actively retained in the $CD45^+$ cells, with positive
263 rates exceeding 65% in all treated mice (Fig. 5g). Among the $CD45^+$B5-$D3^+$ cells, more than 95%
264 were macrophages, composed primarily of $CD11c^+$Siglec-F^+ AMs (87.2 – 91.7%) and Siglec-F^-
265 $CD11b^-$F4/80^+ monocyte-derived macrophages (mono-Macs; 6.6 – 9.9%) (Fig. 5h, red arrows).
266 Consistently, these macrophage populations also exhibited the highest B5-D3 positive rates (Fig.
267 5i,j; Supplementary Fig. 13) and greatest median fluorescent intensities (MFI) (Fig. 5k, red arrows)
268 among all immune cell types in the BALF, indicating the strongest B5-D3-AF750 uptake. Other
269 phagocytic cell types such as the type 2 conventional dendritic cells (cDC2) and monocytes also
270 exhibited considerable AF750 intensities (Fig. 5k, blue arrows; Supplementary Fig. 13b,c),
271 suggesting potential relationships between B5-D3 uptake and phagocytic activities. Confocal
272 microscopy of BALF cells after immunostaining further confirmed that the B5-D3-AF750 were
273 present in the cytoplasm after being retained in AMs (Fig. 5l). These results demonstrate that IN B5-
274 D3 preferentially accumulates in the respiratory tract and is predominantly taken up by airway
275 macrophages, supporting their important role in mediating early immune responses.

276

277 **sACE2-Fc facilitates phagocytosis of SARS-CoV-2 pseudovirus via mechanisms distinct from**
278 **ACE2-dependent viral infection**

279 To examine the implication of macrophage involvement in the early immune activation observed in
280 IN B5-D3 treatment groups, we performed cellular analysis using THP-1 cells as an *in vitro* model
281 for phagocytes [41] and examined the sACE2-Fc-dependent phagocytosis of spike-pseudotyped
282 lentiviruses. Indeed, immunostaining of HIV capsid protein p24 confirmed the attachment and entry
283 of pseudoviruses in the THP-1 cells in a B5-D3-dependent manner, with an evidenced signal peak
284 at 6 h post-co-incubation (Supplementary Fig. 14). Interestingly, analysis on the THP-1-derived M0
285 and M1 macrophages detected even greater p24 signals, indicating stronger phagocytosis activities
286 compared to undifferentiated THP-1 cells (Fig. 6a,b; Supplementary Fig. 15a,b,d,e). This process
287 resembled antibody-dependent cellular phagocytosis (ADCP), which is significant in THP-1-
288 derived M0 and M1 macrophages [42]. Consistently, further examination revealed colocalization of
289 internalized pseudovirus with lysosomal associated membrane protein 1 (LAMP1), indicating
290 trafficking to lysosomes potentially for degradation [43] (Fig. 6c; Supplementary Fig. 15c,f).

291 We further examined the pseudovirus uptake in Calu-3 cells overexpressing human ACE2 (hACE2-
292 Calu-3; Supplementary Fig. 16) as a model of lung epithelial cells. In contrast to that in macrophages,
293 co-incubation with B5-D3 significantly reduced the pseudovirus entry in hACE2-Calu-3 cells (Fig.
294 6d–f). Interestingly, while the pseudovirus transduction in hACE2-Calu-3 cells, in the absence of
295 B5-D3, produced robust luciferase signal indicating viral genome release after cell entry, the evident
296 pseudovirus uptake facilitated by B5-D3 in the THP-1 and derivative macrophages yielded no
297 detectable luciferase activity, which further supported viral degradation within phagolysosomes (Fig.
298 6g). Corroborating these observations, western blot analysis showed absence of cleaved S2′

fragments in the macrophages that had internalized pseudovirus-B5-D3 complexes, supporting that the pseudoviruses did not undergo membrane fusion or cytosolic release as it did in the epithelial cell model [44] (Fig. 6h).

To evaluate the contribution of Fc-mediated effector functions to virus uptake in macrophages, we further compared the efficiencies of B5-D3, B5-D3-LALA, and hIgG1 isotype in mediating pseudovirus uptake by THP-1-derived macrophages (Supplementary Fig. 17). As indicated by p24 staining, functional impairment (LALA mutations) of Fc in B5-D3 significantly reduced the efficiency of virus uptake, emphasizing the importance of intact Fc in B5-D3 function as decoy. Whereas presence of hIgG1 isotype control showed no impact on pseudovirus uptake, supporting that the phagocytosis was largely specific to the pseudovirus-decoy complexes.

To further evaluate the responses triggered by the pseudovirus-B5-D3 complex in macrophages, we performed RNA-seq analysis. The transcriptomic profiling revealed little difference and identified no DEG between the macrophages incubated with both pseudovirus and B5-D3 and those treated with pseudovirus only (Supplementary Fig. 18a). Whereas interestingly, GSEA detected broad activation of pathways related to antiviral response and macrophage activation in the macrophages internalizing pseudovirus and B5-D3 (Supplementary Fig. 18b–i), corresponding to ADCP effect. These findings indicate moderate immune activation triggered by phagocytosis of pseudovirus-decoy complexes, corroborating with the mild immune activation that accelerated antiviral responses in our mice infection experiments.

Collectively, these findings suggest that IN B5-D3 not only blocks viral entry into epithelial cells but also actively redirects SARS-CoV-2 to phagocytic clearance by engaging airway phagocytes via Fc-dependent mechanisms. Moreover, such ADCP-like process contributes to early immune activation and restricts the infection at the respiratory mucosal surface.

322

323 **DISCUSSION**

324 In this study, we comprehensively evaluated the protective efficacy and mechanistic basis of an
325 optimized representative sACE2-Fc decoy (B5-D3) against SARS-CoV-2 infection. By introducing
326 only two mutations (T92Q and H374N), we generated a minimally engineered sACE2-Fc mutant
327 (B5-D3) that achieved broad-spectrum neutralization with minimal risk of disrupting the RAS.
328 Among various administration routes and dosing schedules examined, we demonstrated that IN
329 prophylaxis of B5-D3 achieved the most robust protection, completely preventing disease in both
330 young and aged K18-hACE2 mice. Transcriptomic analysis of the infected lung samples at early
331 time points revealed distinct IN B5-D3-dependent immune activation at the onset of infection,
332 indicating that B5-D3 acted not only as a receptor decoy but also as an immune engager upon viral
333 infection. Bio-distribution analysis of fluorescence-labeled B5-D3 demonstrated rapid uptake and
334 high accumulation in the respiratory tract, primarily within airway macrophages. Phagocytosis
335 assays further supported that sACE2-Fc decoy mediated a rapid viral clearance in macrophages,
336 while abolishing membrane ACE2-mediated infection in epithelial cells. Together, these findings
337 reveal a dual-function mechanism for sACE2-Fc decoys in redirecting SARS-CoV-2 to phagocytic
338 clearance and rapid immune engagement, supporting their potential as intranasal prophylactics
339 against respiratory viruses.

340 Previous studies have reported multiple ACE2 mutations with remarkable potential in neutralizing
341 SARS-CoV-2. However, in these studies, combining ACE2 mutations based on *in silico* predictions
342 to both enhance spike binding and eliminate the ACE2 enzymatic activity in a single design resulted
343 in accumulation of mutations such as K31F/N33D/H34S/E35Q/H345L [12] and
344 L79F/M82Y/Q325Y/H374A/H378A [14]. These extensive mutations have been implicated in

345 structural instability [12] and reduced production efficiency [17]. More importantly, the high
346 mutation loads raise risks for immunogenicity, which is a critical issue when considering clinical
347 applications. Corroboratively, Urano *et al.* detected *in vitro* T cell stimulation elicited by the L79F
348 mutation, whereas the T92Q mutation showed much lower immunogenicity and enhanced spike
349 binding affinity [45]. In our ACE2 decoy design, we incorporated only two mutations (like T92Q
350 and H374N in B5-D3) to enhance neutralization potency while eliminating enzymatic activity,
351 resulting in simplest compound ACE2 mutants. The B5-D3, as a representative, exhibited not only
352 minimal mutation-related risks but also top-level neutralization potencies among all candidate
353 mutants we tested. Hnece, by coupling structural engineering (Fc fusion for avidity improvement)
354 and mutagenesis (potency and safety optimization), we provided simplest decoy design and further
355 consolidated the generalizable framework for decoy design, which is invaluable to combat a novel,
356 highly contagious, and fatal virus in future, before more effective vaccines and drugs are established.

357 Previous studies have reported that IN prophylaxis with sACE2-Fc mutants or monoclonal
358 antibodies [15, 16, 46] could effectively protect against SARS-CoV-2, in which the Fc-effector
359 functions were indispensable [14]. However, the precise mechanism has not been well depicted,
360 which prevents the further development of these approaches for translation. Here, our study provided
361 evidence for a deeper mechanistic insight, showing that IN sACE2-Fc decoys rapidly engage host
362 immunity in the respiratory tract. Consistently with others' work [14], IN delivery of a Fc-null
363 variant (B5-D3-LALA) resulted in suboptimal protection and higher viral infection compared to B5-
364 D3. Notably, despite the minimal infection observed, B5-D3-treated mice showed robust early
365 immune activation, including induction of antigen presentation and T cell activation within 24 h
366 post-infection (Fig 4). These results support that B5-D3 not only neutralizes virus but also primes
367 innate and adaptive immune responses, counteracting early-stage viral immune evasion.

368 Furthermore, our bio-distribution data showed that IN-delivered B5-D3 preferentially accumulates
369 in the respiratory tract (Fig. 5a–d). Flow cytometry and confocal imaging confirmed strong binding
370 and uptake of B5-D3 by airway phagocytes, primarily alveolar macrophages and monocyte-derived
371 macrophages (Fig. 5e–l). Notably, phagocytosis assays demonstrated that B5-D3–virus complexes
372 were trafficked to lysosomes for degradation in macrophages. Functional impairment in the B5-D3
373 structure reduced the uptake of virus by macrophages. These findings support a mechanism in which
374 B5-D3 redirects viral particles away from membrane ACE2-dependent epithelial entry and toward
375 phagocytic clearance (Fig. 7). Importantly, RNA-Seq analysis of macrophages treated with virus-
376 decoy complexes suggests that such ADCP-like process also facilitated early immune activation and
377 initiated downstream antiviral signaling cascades before the virus reaches epithelial targets (Fig. 7b).
378 Hence, the IN prophylaxis offers a unique advantage by enabling localized immune priming and
379 efficient viral clearance at the frontline of infection. The IN-administered antibody drugs can share
380 similar mechanism and confer effective protection against primary infection of SARS-CoV-2 or
381 other respiratory viruses. However, antibody drugs can be easily escaped when new viral variants
382 emerge, which is specifically common among rapidly spreading respiratory RNA viruses [47]. In
383 contrast, the decoy strategy is intrinsically resistant to "antigenic escape" of the mutating virus,
384 which is further supported by the trend observed in viral evolution that later-emerging SARS-CoV-
385 2 variants exhibit a higher affinity for the ACE2 receptor, enhancing their infectivity and
386 transmissibility [16].

387 In a post-infection context, respiratory viruses would have propagated extensively at the primary
388 infection site when symptoms arise, which makes IN neutralization relatively ineffective to clear the
389 high viral burden and the resultant systematic inflammation [48]. Therefore, the therapeutic activity
390 of either local or systemic neutralization at post-infection stage is bound to be restricted, which is
391 intrinsically inherited in all decoy/antibody therapies against respiratory viral infections. Yet,

392 transfusion of convalescent plasma or infusion of neutralizing mAbs in clinical practice have been
393 shown to reduce the mortality in COVID-19 [49, 50], and IV administration of B5-D3 as therapy
394 was also shown effective in improving the viral burden and survival in our aged mouse experiment
395 (Fig. 2a–e). Therefore, the therapeutic value of our decoy strategy does exist when a "systematic"
396 route of administration (*e.g.*, IV infusion) is chosen, and improvement in disease severity should
397 thus be expected.

398 Our study has several limitations. First, we didn't examine the potential of IgM-based sACE2
399 decamers, which showed higher avidity to spikes and greater potency for viral neutralization in
400 previous studies [46, 51, 52]. It is promising that our B5-D3 design would benefit from switching
401 to the IgM isotype, whereas the distinct biological features imposed by IgM Fc, including short
402 serum half-life and restricted tissue penetration [53], may complicate the analysis design and diverge
403 our study focus. Moreover, although no sign of B5-D3-specific immune responses was observed in
404 our AAV-injected mice, its immunogenicity and potential risk for antibody-dependent enhancement
405 (ADE) should be thoroughly evaluated to further develop the decoy strategy for human use.
406 Furthermore, despite that K18-hACE2 mice are broadly used and demonstrate the best susceptibility
407 to SARS-CoV-2 infection among established hACE2-transgeic mouse models [54], hACE2
408 expression in these mice shows a distinct pattern that may not reflect human physiology [31, 55].
409 Further study on hACE2 decoy using animals with physiological level of hACE2 expression and
410 humanized immune system that can support stable engraftment of myeloid lineages would be
411 warranted.

412 In conclusion, we present a rationally designed sACE2-Fc decoy with minimal mutagenesis (B5-
413 D3) and provide compelling evidence and insights into the immune mechanism supporting its potent
414 prophylactic efficacy. Intranasal prophylactic administration of B5-D3 not only neutralizes SARS-

415 CoV-2 but also redirects the virus toward phagocytic clearance, enabling early immune engagement
416 and complete protection. These findings provide a mechanistic basis for decoy-based antiviral
417 strategies and offer a promising approach to combat current and future airborne viral threats. Further
418 studies may aim to develop approaches to enhance the rapid local immune engagement to restrict
419 early viral propagation. Additionally, regimen refinements are needed to enhance stability and
420 functionality of decoy-based treatments before their clinical translation and extension to a broader
421 range of respiratory pathogens.

422

423 **MATERIALS AND METHODS**

424 **Plasmid construction**

425 The coding sequence of human ACE2 was cloned into the pGEM-T easy vector (Promega) and
426 underwent site-directed mutagenesis [10-12, 17]. The sACE2 and human IgG1 hinge-Fc regions (aa
427 216-447) were assembled via overlapping PCR. These constructs, along with 6xHis-tagged versions,
428 were inserted into the HDM-SARS2-Spike-delta21 vector (Addgene #155130) to generate HDM-
429 CMV-sACE2(-Fc)-his plasmids. L234A/L235A (LALA) in hIgG1 were introduced to generate
430 HDM-CMV-sACE2-Fc-LALA-his plasmids. Various sACE2-Fc fragments were then subcloned
431 into pAAV-nEFCas9 vector (Addgene #87115) to generate AAV-nEF-sACE2-Fc plasmids. SARS-
432 CoV-2 spike variants with or without an HA tag fused to the C-terminal were synthesized and
433 inserted into the HDM vector [56].

434 **Protein structure visualization**

435 The crystal structure of SARS-CoV-2 spike receptor-binding domain bound with ACE2 (6M0J) was
436 downloaded from the Protein Data Bank (PDB, https://www.rcsb.org/structure/6m0j) [57]. Color-

437 labeling of individual amino acids was performed on the PDB website. For structural overlapping
438 analysis of WT sACE2 and B5-D3 (aa 18-740), protein structures were predicted using online
439 AlphaFold 3 server (https://alphafoldserver.com/) [22]. PyMOL was utilized for root mean square
440 deviation (RMSD) calculations and structural visualization.

441 **Cell culture**

442 293T, Vero E6, Calu-3, and THP-1 cells were obtained from the American Type Culture Collection
443 and incubated at 37 °C with 5% CO_2. Specifically, 293T, Vero E6, and Calu-3 cells were maintained
444 in Dulbecco's Modified Eagle Medium (DMEM, Gibco) supplemented with 10% fetal bovine serum
445 (FBS, Gibco) and 1% Penicillin-Streptomycin (PS, Gibco). THP-1 cells were cultured in Roswell
446 Park Memorial Institute 1640 medium (RPMI, Gibco) with similar supplements. THP-1 cells were
447 differentiated into M0 macrophages using 50 nM phorbol 12-myristate 13-acetate (PMA) for 48 h,
448 followed by a 24 h rest. For M1 macrophage differentiation, post-PMA treatment cells were
449 stimulated with 10 ng/mL lipopolysaccharide and 20 ng/mL interferon (IFN)-γ for 24 h. Expi293
450 cells (Gibco) were cultured following the manufacturer's instructions.

451 **Immunofluorescence staining of hACE2-293T and hACE2-Calu-3**

452 Cells were fixed, permeabilized, and blocked with 10% Normal Goat Serum (Invitrogen). ACE2
453 was stained with a primary antibody (Abcam #ab15348) followed by an Alexa Fluor 594-conjugated
454 secondary antibody (Invitrogen #A-21442). Cells were counterstained with Hoechst 33342 (Thermo
455 Scientific) and examined under Nikon Ti2-E Inverted Fluorescence Microscope.

456 **Lentivirus packaging and transduction**

457 293T cells were seeded at 80% confluence and transfected with psPAX2 (Addgene #12260),
458 pMD2.G (Addgene #12259), and transfer plasmid pWPI-IRES-Puro-Ak-ACE2-TMPRSS2

459 (Addgene #154987) using polyethylenimine (PEI). Lentivirus-containing medium was harvested 72
460 h post-transfection, filtered through a 0.45 μM filter, concentrated, and stored at -80°C. For
461 transduction, 293T or Calu-3 cells were exposed to the concentrated lentivirus with 8 μg/mL
462 polybrene for 24 h to obtain human ACE2-overexpressing cell lines (hACE2-293T and hACE2-
463 Calu-3 respectively).

464 **Pseudovirus packaging, titration, and infection**

465 Pseudoviruses were packaged in 293T cells using pCDH-EF1a-eFFly-eGFP (Addgene #104834)
466 and spike-encoding plasmids, following a similar protocol to that of lentivirus. Post-packaging,
467 pseudoviral particles were titrated using the Lenti-X qRT-PCR Titration Kit (Takara #631235) and
468 used to infect target cells in the presence of 8 μg/mL polybrene. Infectivity was assessed via a
469 luciferase assay (Promega #E1501).

470 **Protein production and purification**

471 293T and Expi293 cells were transfected with HDM-CMV-sACE2(-Fc)(-LALA)-his plasmids using
472 PEI and ExpiFectamine 293 Transfection Kit (Gibco) respectively. Culture supernatants were
473 collected after 72 h and 5 days post-transfection respectively. The 293T supernatant was assessed
474 for ACE2 and IgG1 levels using enzyme-linked immunosorbent assay (ELISA) kits (Abcam
475 #ab235649; Invitrogen #BMS2092), and ACE2 activity was measured with a fluorometric assay
476 (Abcam # ab273297). The Expi293 supernatant underwent Ni-NTA Agarose purification, followed
477 by elution and buffer exchange to phosphate-buffered saline (PBS, pH 7.4). Protein concentration
478 and integrity were verified using the Bradford method, ELISA, and sodium dodecyl sulfate-
479 polyacrylamide gel electrophoresis (SDS-PAGE).

480 ***In vitro* pseudovirus neutralization assay**

481 Conditioned media containing sACE2, sACE2-Fc or sACE2-Fc-LALA proteins were diluted
482 serially, mixed with pseudovirus (4×10^9 copies), and incubated at room temperature for 30 minutes
483 [19]. The mixture was added to hACE2-293T cells in 96-well plates with duplicates with 8 μg/mL
484 polybrene. Transduction efficiency was assessed 48 h later via green fluorescent protein (GFP)
485 imaging and/or luciferase assays.

486 **Reporter-based *in vitro* ADCC and ADCP assays**

487 The *in vitro* antibody-dependent cell-mediated cytotoxicity (ADCC) and antibody-dependent
488 cellular phagocytosis (ADCP) activities of B5-D3(-LALA) were measured using Jurkat-Lucia
489 NFAT-CD16 and Jurkat-Lucia NFAT-CD32 cells (InvivoGen) respectively according to the
490 manufacturer's instructions. 293T cells transfected with pBOB-CAG-SARS-CoV-2-Spike-HA
491 (Addgene #141347) acted as target cells. Target cells were co-incubated with reporter cells and
492 serially diluted B5-D3(-LALA) at 37°C for 1 h. Luciferase expression indicating CD16 and CD32
493 signaling was measured using QUANTI-Luc (InvivoGen).

494 **ADCP of pseudovirus** in THP-1 and THP-1-derived macrophages

495 SARS-CoV-2 pseudovirus (Wuhan-Hu-1, 8×10^8 copies in 10 μL) was mixed with 50 μL of B5-D3
496 or control proteins (20 μg/mL) and added to THP-1, M0, or M1 cells cultured in a μSlide 18 Well
497 iBITreat chamber slide. Here THP-1 cells were attached on the collagen-coated iBITreat chamber
498 slide. After 1, 3, 6, or 18 hours of incubation for phagocytosis, cells were fixed with ice-cold
499 methanol for 10 minutes, blocked with 10% normal goat serum for 1 hour at room temperature, and
500 immunostained sequentially for human IgG-Fc (Abcam #ab98596), HIV-1 p24 (Invitrogen #PA5-
501 81773), and lysosomal associated membrane protein 1 (LAMP1) (Abcam #ab25630). Secondary
502 antibodies were applied (Invitrogen #A-21200 and #A-31573), and nuclei were stained with Hoechst.

503 Imaging was conducted using a Leica SP8 confocal microscope. p24 immunofluorescence intensity
504 and colocalization with LAMP1 (Manders' coefficient) were analyzed using ImageJ and the JACoP
505 plugin.
506 For RNA extraction, M0 cells were washed once with PBS and added with TRIzol (Invitrogen) after
507 6 h incubation with pseudovirus with/without B5-D3 (n = 3 in triplicate wells).

508 **Western blot for spike cleavage detection**

509 SARS-CoV-2 spike-HA tagged pseudovirus (4×10^9 copies) was incubated with M0/M1
510 macrophages or hACE2-293T cells for 6 h, with or without sACE2-Fc proteins. After incubation,
511 cell lysates were processed through SDS-PAGE and transferred to polyvinylidene difluoride
512 membranes. The membranes were blocked, incubated overnight with anti-HA (Merck Millipore
513 #05-904) and anti-β-actin (Santa Cruz #sc-47778) primary antibodies, then with horseradish
514 peroxidase (HRP)-conjugated secondary antibodies (Cell Signaling Technology #7076). Signals
515 were detected using the Amersham ECL select kit on a Bio-Rad ChemiDoc MP system.

516 **AAV vector packaging and purification**

517 As described previously [58], AAV vectors were produced in 293T cells transfected with AAV-nEF-
518 sACE2-Fc, pAdDeltaF6 (Addgene #112867), and pAAV2/8 (Addgene #112864) plasmids using PEI.
519 AAV particles were harvested from supernatants with Polyethylene Glycol (PEG) 8000 and from
520 cell lysates via freeze-thaw cycles and benzonase digestion, then purified using Iodixanol density
521 gradient ultracentrifugation. AAV particles were concentrated and measured using a qPCR AAV
522 Titer Kit (Applied Biological Materials #G931).

523 **SARS-CoV-2 virus**

524 Experiments with live SARS-CoV-2 were performed at the BSL-3 core facility (LKS Faculty of

525 Medicine, HKU). The BetaCoV/Hong Kong/VM20001061/2020 virus, here regarded as the wild
526 type strain of SARS-CoV-2 (Wuhan-Hu-1), was isolated from the nasopharyngeal aspirate and throat
527 swab of a confirmed patient with COVID-19 in Hong Kong (GISAID identifier EPI_ISL_412028).
528 The SARS-CoV-2 variants were isolated from clinical specimens in Hong Kong. Stock viruses were
529 prepared with Vero E6 cells cultured in infection medium (DMEM supplemented with 2% FBS and
530 1% PS).

531 **Median tissue culture infectious dose ($TCID_{50}$) assay**

532 Vero E6 cells pre-seeded in 96-well plates were infected with serially diluted virus stocks or mouse
533 lung homogenates in infection medium. After 72 h incubation, cytopathic effects (CPEs) were
534 observed under a microscope to calculate titers using the Reed–Muench method.

535 **Plaque-reduction neutralization test (PRNT) assay**

536 Casirivimab (#C100P) and hIgG1 isotype (clone 4F17, #PA007125) were purchased from Syd Labs,
537 USA) and used as controls. Purified B5-D3 and control proteins were serially diluted and incubated
538 with 50 PFU of SARS-CoV-2 (Wuhan-Hu-1, Delta, Omicron BA.5, BQ.1.22, and XBB.1.5) for 1 h
539 at room temperature, followed by addition to Vero E6 cells seeded in 6-well plates. After incubation,
540 cells were overlaid with agarose, fixed with formalin, and stained with crystal violet. Plaque counts
541 were used to calculate percentage neutralization and half maximal inhibitory concentration (IC_{50})
542 values. The experiments were carried out in duplicates.

543 **Animal experiments**

544 The K18-hACE2 mice (B6.Cg-Tg(K18-ACE2)2Prlmn/J) [31] were purchased from the Jackson
545 Laboratory (Bar Harbor, ME, USA). Experiments on AAV or protein-only administration in mice
546 were carried out in the Animal Holding Core of the School of Biomedical Sciences, CUHK.

547 Experiments involving SARS-CoV-2 infection in K18-hACE2 mice were conducted within the
548 confines of the Biosafety Level 3 (BSL-3) core facility located at the Li Ka Shing Faculty of
549 Medicine, HKU. Experiments were conducted according to ethical practices to minimize animal
550 distress.

551 **AAV-mediated sACE2-Fc overexpression in mice**

552 Male K18-hACE2 mice [31] at the age of 2 months were injected intravenously with 1×10^{11} GC
553 of AAV-nEF-sACE2-Fc. Blood samples were collected periodically for analysis. Following
554 euthanasia, tissues were harvested for further DNA and histological analysis. sACE2-Fc
555 concentrations in sera and RAS metabolites were quantified using specific ELISA kits for Human
556 IgG1, Mouse Renin 1 (Invitrogen #EMREN1), Angiotensin II (LifeSpan BioSciences #LS-F523),
557 and Angiotensin 1-7 (LifeSpan BioSciences #LS-F40645).

558 **SARS-CoV-2 infection in mice**

559 Female K18-hACE2 mice, aged 10-12 months or 2-3 months, were intranasally inoculated with
560 1×10^4 plaque-forming unit (PFU) of SARS-CoV-2 Wuhan-Hu-1. Treatment with B5-D3 protein was
561 administered intranasally at 2.5 mg/kg or intravenously at 15 mg/kg, at various time points relative
562 to the viral challenge (6 h before, 24 h before, or 24 h after). Vehicle control groups received PBS 6
563 h before viral challenge. Survival and weight were monitored daily for 14 days. For the older mice,
564 lung samples were collected from one mouse from each group at 4 days post-infection (dpi) for
565 analysis; younger mice had plasma collected for neutralizing antibody analysis at 14 dpi. Another
566 batch of young mice also received B5-D3(-LALA) protein pre-inoculation, with lungs analyzed
567 post-inoculation for RNA, viral load, and histopathology. A control group of non-infected mice was
568 used to assess baseline effects of B5-D3 on lung tissue.

569 **Neutralization assay for antibody titration**

570 Vero E6 cells were pre-seeded on 96-well plates 24 h before infection. On the day of infection, the
571 growth medium of the cells was changed to infection medium. The plasma samples were serially 2-
572 fold diluted with infection medium from a starting dilution of 1:10. The plasma was then pre-
573 incubated with 100 $TCID_{50}$ of SARS-CoV-2 for 1 h at room temperature before being inoculated to
574 the seeded Vero E6 cells in quadruplicates. At 72 h after inoculation, CPEs of the cells were observed
575 with optical microscopy. Neutralizing antibody titers against SARS-CoV-2 were expressed as the
576 reciprocal of the highest dilution of plasma showing no CPEs in all 4 wells. Uninfected cell
577 monolayers were used as toxicity control.

578 **Histology**

579 Mouse tissues were fixed in 10% formalin, embedded in paraffin, and sectioned at 5 μm. Sections
580 of different organs were deparaffinized and underwent hematoxylin and eosin (H&E) staining. For
581 immunohistochemistry (IHC) staining, lung sections underwent antigen retrieval, endogenous
582 peroxidase blocking, and were incubated with primary antibodies against the SARS-CoV/SARS-
583 CoV-2 nucleocapsid protein (Sino Biological #40143-T62) overnight. After washing, sections were
584 stained with the anti-rabbit VECTASTAIN Elite ABC-HRP Kit (Vector Laboratories), developed
585 with 3,3′-Diaminobenzidine (Sigma #D4293), and counterstained with Mayer's hematoxylin.
586 Stained sections were scanned using Zeiss Axioscan 7 and analyzed using ZEN (blue edition). For
587 measurement of alveolar septal thickness, 10 fields from each lung H&E section and 10 septa from
588 each field were chosen for measurement using ImageJ.

589 **Quantitative PCR**

590 Quantitative PCR (qPCR) was used to analyze liver genomic DNA and lung RNA from mice. DNA
591 was extracted and qPCR was performed with the TB Green Premix Ex Taq II kit (Takara),
592 normalized to mouse *Gapdh* using the 2^-ΔCt method. RNA was extracted using TRIzol, reverse-

593 transcribed (Applied Biosystems #4368813), subjected to qPCR using the same kit and normalized
594 to mouse *Gapdh* levels. Specific primers are listed in Supplementary Table 2.

595 **RNA-Seq and data analysis**

596 Total RNA was extracted from mouse lung tissues or THP-1-derived M0 macrophages using TRIzol
597 and processed into transcriptome libraries with the TruSeq RNA Library Prep Kit (illumina).
598 Sequencing was performed on the NovaSeq 6000 or NovaSeq X Plus sequencers (illumina) using a
599 150-base pair paired-end configuration. Sequencing data were processed with fastp for quality
600 control [59], then aligned to both the mouse (Ensembl GRCm39) and SARS-CoV-2 (NCBI
601 NC_045512v2) genomes using STAR [60] or to the human genome (Ensembl GRCh38) using
602 HISAT2 [61]. Pearson correlation and groupwise comparisons were conducted in R: gene
603 expression was quantified and analyzed for differential expression using DESeq2 [62];
604 up/downregulated gene enrichment and Gene Set Enrichment Analysis (GSEA) [63] was performed
605 using the clusterProfiler package [64].

606 **Tracking B5-D3 bio-distribution in mice**

607 B5-D3 were conjugated with Alexa Fluor 750 dye (B5-D3-AF750) as described [46]. In brief, 2
608 mg/mL solution of B5-D3 protein in 0.15 M $NaHCO_3$ was reacted with Alexa Fluor 750
609 succinimidyl ester (Thermo Fisher Scientific) at room temperature for 1 h. Unreacted dye was
610 removed by dialysis in PBS. All procedures were performed under dimmed light. Female K18-
611 hACE2 mice, aged 2-3 month, were administered intranasally with B5-D3-AF750 (2.5 mg/kg). The
612 mice were imaged at predetermined time points after administration (fluorescence ex = 745 nm,
613 em = 800 nm, auto-exposure setting) using an IVIS Spectrum CT Imager (Perkin Elmer). At the
614 time of euthanasia, 50 μL of urine and blood, the brain, nasal cavity, trachea, lung, heart, liver, spleen,
615 kidney, and urinary bladder samples were excised and imaged. Regions of interest (ROIs) were

616 drawn, and average radiance (p/s/cm²/sr) was measured. All images were processed using Living
617 Image software (Perkin Elmer) and the same fluorescence threshold was applied for group
618 comparison.

619 **Flow cytometry analysis and confocal microscopic imaging of BALF cells**

620 Mice were sacrificed via anesthetics overdose. Bronchoalveolar lavage was performed by
621 intratracheally rinsing the lungs with 1 mL of ice-cold Hanks' Balanced Salt Solution (HBSS, Gibco)
622 containing 100 μM ethylenediaminetetraacetic acid for four repeats. Bronchoalveolar lavage fluid
623 (BALF) was then centrifuged and treated with ammonium-chloride-potassium red blood cell lysing
624 buffer. For multicolor flow cytometry, cell pellets were washed with PBS and stained with the
625 Fixable Viability Stain 440UV dye (BD #566332). Next, the cells were blocked with CD16/CD32
626 monoclonal antibody (Invitrogen #14-0161-85) and stained with antibodies targeting the following
627 molecules: CD45 (BD #568336), Siglec-F (BD #564514), CD11b (BD #612800), CD11c (BD
628 #751265), Ly6G (BD #563005), I-A/I-E major histocompatibility complex class II (MHC-II) (BD
629 #750171), F4/80 (BD #570288), Ly6C (BD #755198), and CD3 (BD #555275). Stained BALF cells
630 were analyzed using the BD FACSymphony A5.2 SORP Flow Cell Analyzer, and the results were
631 analyzed using FlowJo v10.10.

632 For microscopic inspections, BALF cells were collected from mice, seeded in poly-d-lysine-coated
633 chamber slides and stained with antibodies targeting Siglec-F (BD #564514) and human IgG-Fc
634 (Abcam #ab98596). Secondary antibody (Invitrogen #A-11006) was applied. Stained BALF cells
635 were then counterstained with Hoechst and examined by confocal microscopy (Leica TCS SP8).

636 **Statistical Analysis**

637 Assays including *in vitro* neutralization, PRNT, ADCC, and ADCP were conducted in technical
638 duplicates. Results were analyzed in GraphPad Prism version 9 using nonlinear regression to

639 calculate IC_{50} or half maximal effective concentration (EC_{50}) values. Transcriptomic analyses were
640 performed using R, with details provided in figure captions. All other statistical analyses utilized
641 GraphPad Prism version 9 with a significance threshold set at *p* value (*p*) < 0.05.

642

643 **SUPPLEMENTARY INFORMATION**

644 This PDF file includes:

645 Fig. S1 to S18; Tables S1 and S2.

646

647 **DECLARATIONS**

648 **Ethics approval and consent to participate**

649 All animal procedures were ethically approved by The Chinese University of Hong Kong (CUHK)'s
650 Animal Experimentation Ethics Committee (approval number: 20-226-MIS) and The University of
651 Hong Kong (HKU)'s Committee on the Use of Live Animals in Teaching and Research (approval
652 number: 5511-20).

653 **Availability of data and materials**

654 All data associated with this study are available in the main text or the supplementary materials. The
655 RNA-seq data generated in this study have been deposited in the NCBI Sequence Read Archive
656 database under accession code PRJNA1054508. Constructs of diverse sACE2-Fc mutants and
657 SARS-CoV-2 spikes are available upon request after completion and approval of a material transfer
658 agreement by contacting fengbo@cuhk.edu.hk.

659 **Competing interests**

660 The authors declare that they have no competing interests.

661 **Funding**

662 This study was supported by Research Grants Council of Hong Kong grants 14115520, 14106024
663 (B.F.), C7145-20GF (L.L.P.), and in part by the Health@InnoHK Program launched by Innovation
664 Technology Commission of the Hong Kong SAR, China. Jingyi W., J.L, B.L., and J.Q. received
665 postgraduate studentships from the Chinese University of Hong Kong.

666 **Authors' contributions**

667 Jingyi W. and J.L. constructed the sACE2-Fc mutants and performed characterization analysis;
668 A.W.C. performed the PRNTs and data analysis; Jingyi W., A.W.C., and J.L. performed the mouse
669 infection experiments and data analysis; B.L., J.Q. and J.R. produced recombinant sACE2-Fc
670 proteins; Jingyi W. and Junkang W. performed RNA-Seq analysis; Jingyi W. and J.Q. performed
671 protein labeling, *in vivo* tracing of labeled protein, and flow cytometry analysis of BALF cells; J.L.
672 performed THP-1 and Calu-3 experiments and confocal microscopic analysis. Junkang W. and J.L.
673 performed protein structure prediction and visualization. Jingyi W., J.L., L.L.P. and B.F. conceived
674 the project, designed experiments, and wrote the manuscript. Y.X., T.B., L.L.P. and B.F. revised the
675 manuscript. All authors read and approved the final manuscript.

676 **Acknowledgements**

677 We thank the Chinese University of Hong Kong (CUHK) and the University of Hong Kong (HKU)
678 research platforms for assistance in animal experimentation (the Laboratory Animal Service Center
679 at CUHK and the Centre for Comparative Medicine Research at HKU) and histological analysis
680 (Department of Pathology, HKU and Core Laboratory in the School of Biomedical Sciences,
681 CUHK).

682

REFERENCES

[1] Q. Wang *et al.*, "Alarming antibody evasion properties of rising SARS-CoV-2 BQ and XBB subvariants," *Cell,* vol. 186, no. 2, pp. 279-286.e8, 2023, doi: 10.1016/j.cell.2022.12.018.

[2] M. Hoffmann *et al.*, "SARS-CoV-2 Cell Entry Depends on ACE2 and TMPRSS2 and Is Blocked by a Clinically Proven Protease Inhibitor," *Cell,* vol. 181, no. 2, pp. 271-280.e8, 2020/04/16/ 2020, doi: https://doi.org/10.1016/j.cell.2020.02.052.

[3] S. Ozono *et al.*, "SARS-CoV-2 D614G spike mutation increases entry efficiency with enhanced ACE2-binding affinity," *Nature Communications,* vol. 12, no. 1, p. 848, 2021/02/08 2021, doi: 10.1038/s41467-021-21118-2.

[4] M. Ramanathan, I. D. Ferguson, W. Miao, and P. A. Khavari, "SARS-CoV-2 B.1.1.7 and B.1.351 spike variants bind human ACE2 with increased affinity," *The Lancet Infectious Diseases,* vol. 21, no. 8, p. 1070, 2021, doi: 10.1016/S1473-3099(21)00262-0.

[5] L. Li *et al.*, "Structural basis of human ACE2 higher binding affinity to currently circulating Omicron SARS-CoV-2 sub-variants BA.2 and BA.1.1," *Cell,* vol. 185, no. 16, pp. 2952-2960.e10, 2022, doi: 10.1016/j.cell.2022.06.023.

[6] V. Monteil *et al.*, "Inhibition of SARS-CoV-2 Infections in Engineered Human Tissues Using Clinical-Grade Soluble Human ACE2," *Cell,* vol. 181, no. 4, pp. 905-913.e7, 2020/05/14/ 2020, doi: https://doi.org/10.1016/j.cell.2020.04.004.

[7] A. Zoufaly *et al.*, "Human recombinant soluble ACE2 in severe COVID-19," *The Lancet Respiratory Medicine,* vol. 8, no. 11, pp. 1154-1158, 2020, doi: 10.1016/S2213-2600(20)30418-5.

[8] R. A. S. Santos *et al.*, "The ACE2/Angiotensin-(1-7)/MAS Axis of the Renin-Angiotensin System: Focus on Angiotensin-(1-7)," *Physiol Rev,* vol. 98, no. 1, pp. 505-553, Jan 1 2018, doi: 10.1152/physrev.00023.2016.

[9] P. Liu *et al.*, "Novel ACE2-Fc chimeric fusion provides long-lasting hypertension control and organ protection in mouse models of systemic renin angiotensin system activation," *Kidney International,* vol. 94, no. 1, pp. 114-125, 2018/07/01/ 2018, doi: https://doi.org/10.1016/j.kint.2018.01.029.

[10] Z. Payandeh *et al.*, "Design of an engineered ACE2 as a novel therapeutics against COVID-19," *Journal of Theoretical Biology,* vol. 505, p. 110425, 2020/11/21/ 2020, doi: https://doi.org/10.1016/j.jtbi.2020.110425.

[11] C. Lei *et al.*, "Neutralization of SARS-CoV-2 spike pseudotyped virus by recombinant ACE2-Ig," *Nature Communications,* vol. 11, no. 1, p. 2070, 2020/04/24 2020, doi: 10.1038/s41467-020-16048-4.

[12] A. Glasgow *et al.*, "Engineered ACE2 receptor traps potently neutralize SARS-CoV-2," *Proceedings of the National Academy of Sciences,* vol. 117, no. 45, pp. 28046-28055, 2020, doi: 10.1073/pnas.2016093117.

[13] P. Liu, X. Xie, L. Gao, and J. Jin, "Designed variants of ACE2-Fc that decouple anti-SARS-CoV-2 activities from unwanted cardiovascular effects," *Int J Biol Macromol,* vol. 165, no. Pt B, pp. 1626-1633, Dec 15 2020, doi: 10.1016/j.ijbiomac.2020.10.120.

[14] Y. Chen *et al.*, "Engineered ACE2-Fc counters murine lethal SARS-CoV-2 infection through direct neutralization and Fc-effector activities," *Science Advances,* vol. 8, no. 28, p. eabn4188, 2022, doi: doi:10.1126/sciadv.abn4188.

[15] L. Hassler *et al.*, "Intranasal soluble ACE2 improves survival and prevents brain SARS-CoV-2

infection," *Life Science Alliance,* vol. 6, no. 7, p. e202301969, 2023, doi: 10.26508/lsa.202301969.

[16] D. L. Kober *et al.*, "Development of a mutant aerosolized ACE2 that neutralizes SARS-CoV-2 *in vivo*," *mBio,* vol. 15, no. 6, pp. e00768-24, 2024, doi: doi:10.1128/mbio.00768-24.

[17] K. K. Chan *et al.*, "Engineering human ACE2 to optimize binding to the spike protein of SARS coronavirus 2," *Science,* vol. 369, no. 6508, pp. 1261-1265, 2020, doi: 10.1126/science.abc0870.

[18] J. L. Guy, R. M. Jackson, H. A. Jensen, N. M. Hooper, and A. J. Turner, "Identification of critical active-site residues in angiotensin-converting enzyme-2 (ACE2) by site-directed mutagenesis," *The FEBS Journal,* vol. 272, no. 14, pp. 3512-3520, 2005, doi: https://doi.org/10.1111/j.1742-4658.2005.04756.x.

[19] K. H. D. Crawford *et al.*, "Protocol and Reagents for Pseudotyping Lentiviral Particles with SARS-CoV-2 Spike Protein for Neutralization Assays," *Viruses,* vol. 12, no. 5, p. 513, 2020. [Online]. Available: https://www.mdpi.com/1999-4915/12/5/513.

[20] B. Korber *et al.*, "Tracking Changes in SARS-CoV-2 Spike: Evidence that D614G Increases Infectivity of the COVID-19 Virus," *Cell,* vol. 182, no. 4, pp. 812-827.e19, 2020/08/20/ 2020, doi: https://doi.org/10.1016/j.cell.2020.06.043.

[21] K. Suryamohan *et al.*, "Human ACE2 receptor polymorphisms and altered susceptibility to SARS-CoV-2," *Communications Biology,* vol. 4, no. 1, p. 475, 2021/04/12 2021, doi: 10.1038/s42003-021-02030-3.

[22] J. Abramson *et al.*, "Accurate structure prediction of biomolecular interactions with AlphaFold 3," *Nature,* vol. 630, no. 8016, pp. 493-500, 2024/06/01 2024, doi: 10.1038/s41586-024-07487-w.

[23] W. F. Garcia-Beltran *et al.*, "Multiple SARS-CoV-2 variants escape neutralization by vaccine-induced humoral immunity," *Cell,* vol. 184, no. 9, pp. 2372-2383.e9, 2021, doi: 10.1016/j.cell.2021.03.013.

[24] P. Mlcochova *et al.*, "SARS-CoV-2 B.1.617.2 Delta variant replication and immune evasion," *Nature,* vol. 599, no. 7883, pp. 114-119, 2021/11/01 2021, doi: 10.1038/s41586-021-03944-y.

[25] I. Kimura *et al.*, "The SARS-CoV-2 Lambda variant exhibits enhanced infectivity and immune resistance," *Cell Reports,* vol. 38, no. 2, p. 110218, 2022/01/11/ 2022, doi: https://doi.org/10.1016/j.celrep.2021.110218.

[26] P. J. Halfmann *et al.*, "Characterization of the SARS-CoV-2 B.1.621 (Mu) variant," *Science Translational Medicine,* vol. 14, no. 657, p. eabm4908, 2022, doi: doi:10.1126/scitranslmed.abm4908.

[27] Y. Cao *et al.*, "Omicron escapes the majority of existing SARS-CoV-2 neutralizing antibodies," *Nature,* vol. 602, no. 7898, pp. 657-663, 2022/02/01 2022, doi: 10.1038/s41586-021-04385-3.

[28] S. Wang *et al.*, "Genomic Surveillance for SARS-CoV-2 - China, September 26, 2022 to January 29, 2023," (in eng), *China CDC weekly,* vol. 5, no. 7, pp. 143-151, Feb 17 2023, doi: 10.46234/ccdcw2023.026.

[29] R. Amin, P. Pal, K. Dhama, and T. B. Emran, "Recent update on XBB.1.5 emerging novel mutation of COVID-19," *International Journal of Surgery,* vol. 109, no. 4, pp. 1048-1049, 2023, doi: 10.1097/js9.0000000000000254.

[30] D. M. Weinreich *et al.*, "REGEN-COV Antibody Combination and Outcomes in Outpatients with Covid-19," *New England Journal of Medicine,* vol. 385, no. 23, p. e81, 2021, doi: 10.1056/NEJMoa2108163.

[31] P. B. McCray *et al.*, "Lethal Infection of K18-*hACE2* Mice Infected with Severe Acute Respiratory Syndrome Coronavirus," *Journal of Virology,* vol. 81, no. 2, pp. 813-821, 2007, doi:

doi:10.1128/JVI.02012-06.
[32] V. Dwivedi *et al.*, "Age associated susceptibility to SARS-CoV-2 infection in the K18-hACE2 transgenic mouse model," *Geroscience,* vol. 46, no. 3, pp. 2901-2913, Jun 2024, doi: 10.1007/s11357-024-01102-6.
[33] J. Lund *et al.*, "Human Fc gamma RI and Fc gamma RII interact with distinct but overlapping sites on human IgG," *The Journal of Immunology,* vol. 147, no. 8, pp. 2657-2662, 1991, doi: 10.4049/jimmunol.147.8.2657.
[34] E. S. Winkler *et al.*, "SARS-CoV-2 infection of human ACE2-transgenic mice causes severe lung inflammation and impaired function," *Nature Immunology,* vol. 21, no. 11, pp. 1327-1335, 2020/11/01 2020, doi: 10.1038/s41590-020-0778-2.
[35] Q. Shan *et al.*, "Tcf1 and Lef1 provide constant supervision to mature CD8+ T cell identity and function by organizing genomic architecture," *Nature Communications,* vol. 12, no. 1, p. 5863, 2021/10/06 2021, doi: 10.1038/s41467-021-26159-1.
[36] Y. Yamakita *et al.*, "Fascin1 Promotes Cell Migration of Mature Dendritic Cells," *The Journal of Immunology,* vol. 186, no. 5, pp. 2850-2859, 2011, doi: 10.4049/jimmunol.1001667.
[37] M. Colomer-Molera *et al.*, "Kv1.3-dependent immune system activation is regulated by KCNE4," *Biophysical Journal,* vol. 122, no. 3, p. 14a, 2023, doi: 10.1016/j.bpj.2022.11.302.
[38] M. Rapp *et al.*, "CCL22 controls immunity by promoting regulatory T cell communication with dendritic cells in lymph nodes," *Journal of Experimental Medicine,* vol. 216, no. 5, pp. 1170-1181, 2019, doi: 10.1084/jem.20170277.
[39] Z. R. Korobova, N. A. Arsentieva, and A. A. Totolian, "Macrophage-Derived Chemokine MDC/CCL22: An Ambiguous Finding in COVID-19," *International Journal of Molecular Sciences,* vol. 24, no. 17, p. 13083, 2023. [Online]. Available: https://www.mdpi.com/1422-0067/24/17/13083.
[40] K. Katagiri, M. Hattori, N. Minato, and T. Kinashi, "Rap1 Functions as a Key Regulator of T-Cell and Antigen-Presenting Cell Interactions and Modulates T-Cell Responses," *Molecular and Cellular Biology,* vol. 22, no. 4, pp. 1001-1015, 2002/02/01 2002, doi: 10.1128/MCB.22.4.1001-1015.2002.
[41] W. Chanput, J. J. Mes, and H. J. Wichers, "THP-1 cell line: An in vitro cell model for immune modulation approach," *International Immunopharmacology,* vol. 23, no. 1, pp. 37-45, 2014/11/01/ 2014, doi: https://doi.org/10.1016/j.intimp.2014.08.002.
[42] S. Tedesco *et al.*, "Convenience versus Biological Significance: Are PMA-Differentiated THP-1 Cells a Reliable Substitute for Blood-Derived Macrophages When Studying in Vitro Polarization?," (in English), *Frontiers in Pharmacology,* Original Research vol. 9, 2018-February-22 2018, doi: 10.3389/fphar.2018.00071.
[43] K. Takeda and S. Akira, "Toll-like receptors in innate immunity," *International Immunology,* vol. 17, no. 1, pp. 1-14, 2005, doi: 10.1093/intimm/dxh186.
[44] S. Yu *et al.*, "SARS-CoV-2 spike engagement of ACE2 primes S2′ site cleavage and fusion initiation," *Proceedings of the National Academy of Sciences,* vol. 119, no. 1, p. e2111199119, 2022, doi: doi:10.1073/pnas.2111199119.
[45] E. Urano *et al.*, "An inhaled ACE2 decoy confers protection against SARS-CoV-2 infection in preclinical models," *Science Translational Medicine,* vol. 15, no. 711, p. eadi2623, 2023, doi: doi:10.1126/scitranslmed.adi2623.
[46] Z. Ku *et al.*, "Nasal delivery of an IgM offers broad protection from SARS-CoV-2 variants," *Nature,*

vol. 595, no. 7869, pp. 718-723, 2021/07/01 2021, doi: 10.1038/s41586-021-03673-2.

[47] A. M. Carabelli *et al.*, "SARS-CoV-2 variant biology: immune escape, transmission and fitness," *Nature Reviews Microbiology,* vol. 21, no. 3, pp. 162-177, 2023/03/01 2023, doi: 10.1038/s41579-022-00841-7.

[48] N. R. Cheemarla *et al.*, "Dynamic innate immune response determines susceptibility to SARS-CoV-2 infection and early replication kinetics," *Journal of Experimental Medicine,* vol. 218, no. 8, 2021, doi: 10.1084/jem.20210583.

[49] J. W. Senefeld *et al.*, "COVID-19 Convalescent Plasma for the Treatment of Immunocompromised Patients: A Systematic Review and Meta-analysis," *JAMA Network Open,* vol. 6, no. 1, pp. e2250647-e2250647, 2023, doi: 10.1001/jamanetworkopen.2022.50647.

[50] A. Gupta *et al.*, "Early Treatment for Covid-19 with SARS-CoV-2 Neutralizing Antibody Sotrovimab," *New England Journal of Medicine,* vol. 385, no. 21, pp. 1941-1950, 2021, doi: doi:10.1056/NEJMoa2107934.

[51] J. Liu *et al.*, "An IgM-like inhalable ACE2 fusion protein broadly neutralizes SARS-CoV-2 variants," *Nat Commun,* vol. 14, no. 1, p. 5191, Aug 25 2023, doi: 10.1038/s41467-023-40933-3.

[52] H. Guo *et al.*, "An ACE2 decamer viral trap as a durable intervention solution for current and future SARS-CoV," *Emerging Microbes & Infections,* vol. 12, no. 2, p. 2275598, 2023/12/08 2023, doi: 10.1080/22221751.2023.2275598.

[53] B. A. Keyt, R. Baliga, A. M. Sinclair, S. F. Carroll, and M. S. Peterson, "Structure, Function, and Therapeutic Use of IgM Antibodies," *Antibodies,* vol. 9, no. 4, p. 53, 2020. [Online]. Available: https://www.mdpi.com/2073-4468/9/4/53.

[54] C. Lutz, L. Maher, C. Lee, and W. Kang, "COVID-19 preclinical models: human angiotensin-converting enzyme 2 transgenic mice," *Hum Genomics,* vol. 14, no. 1, p. 20, Jun 4 2020, doi: 10.1186/s40246-020-00272-6.

[55] F. S. Oladunni *et al.*, "Lethality of SARS-CoV-2 infection in K18 human angiotensin-converting enzyme 2 transgenic mice," *Nat Commun,* vol. 11, no. 1, p. 6122, Nov 30 2020, doi: 10.1038/s41467-020-19891-7.

[56] Y. Shu and J. McCauley, "GISAID: Global initiative on sharing all influenza data – from vision to reality," *Eurosurveillance,* vol. 22, no. 13, p. 30494, 2017, doi: doi:https://doi.org/10.2807/1560-7917.ES.2017.22.13.30494.

[57] J. Lan *et al.*, "Structure of the SARS-CoV-2 spike receptor-binding domain bound to the ACE2 receptor," *Nature,* vol. 581, no. 7807, pp. 215-220, 2020/05/01 2020, doi: 10.1038/s41586-020-2180-5.

[58] X. He *et al.*, "Low-dose AAV-CRISPR-mediated liver-specific knock-in restored hemostasis in neonatal hemophilia B mice with subtle antibody response," *Nature Communications,* vol. 13, no. 1, p. 7275, 2022/11/25 2022, doi: 10.1038/s41467-022-34898-y.

[59] S. Chen, Y. Zhou, Y. Chen, and J. Gu, "fastp: an ultra-fast all-in-one FASTQ preprocessor," *Bioinformatics,* vol. 34, no. 17, pp. i884-i890, 2018, doi: 10.1093/bioinformatics/bty560.

[60] N. D. Maulding, S. Seiler, A. Pearson, N. Kreusser, and J. M. Stuart, "Dual RNA-Seq analysis of SARS-CoV-2 correlates specific human transcriptional response pathways directly to viral expression," *Scientific Reports,* vol. 12, no. 1, p. 1329, 2022/01/25 2022, doi: 10.1038/s41598-022-05342-4.

[61] D. Kim, J. M. Paggi, C. Park, C. Bennett, and S. L. Salzberg, "Graph-based genome alignment and genotyping with HISAT2 and HISAT-genotype," *Nature Biotechnology,* vol. 37, no. 8, pp. 907-915, 2019/08/01 2019, doi: 10.1038/s41587-019-0201-4.

[62] M. I. Love, W. Huber, and S. Anders, "Moderated estimation of fold change and dispersion for RNA-seq data with DESeq2," *Genome Biology,* vol. 15, no. 12, p. 550, 2014/12/05 2014, doi: 10.1186/s13059-014-0550-8.

[63] A. Subramanian *et al.*, "Gene set enrichment analysis: A knowledge-based approach for interpreting genome-wide expression profiles," *Proceedings of the National Academy of Sciences,* vol. 102, no. 43, pp. 15545-15550, 2005, doi: doi:10.1073/pnas.0506580102.

[64] T. Wu *et al.*, "clusterProfiler 4.0: A universal enrichment tool for interpreting omics data," *The Innovation,* vol. 2, no. 3, p. 100141, 2021/08/28/ 2021, doi: https://doi.org/10.1016/j.xinn.2021.100141.

FIGURE LEGENDS

Fig. 1 Enhanced sACE2-Fc with two single mutations exhibited broad-spectrum neutralization of SARS-CoV-2 variants. a Schematic representation of sACE2-Fc structure (upper) and neutralization assay setup (lower). Key amino acid positions (90-92 and 374-378) involved in glycosylation and zinc binding are highlighted. Red stars mark the positions of mutations in the sACE2-Fc mutant B5-D3. SP, signal peptide; CLD, collectrin-like domain; hIgG1, human IgG1. **b** Comparative bar graph showing the half-maximal inhibitory concentration (IC_{50}) values for neutralization of Wuhan-Hu-1 and D614G pseudovirues by WT sACE2-Fc and mutants (B2 to B6, A2, A3, D1 to D5, and B5-derivatives). The red arrow emphasizes the superior performance of the B5-D3 mutant. Enzymatic activity of each construct is plotted on the right axis. **c** List of pseudoviruses carrying spikes from different SARS-CoV-2 variants tested, categorized by the World Health Organization (WHO) into VOCs and VOIs. **d** Graph displaying IC_{50} values of WT sACE2-

879 Fc, B5, and B5-D3/4/5 mutants against various SARS-CoV-2 VOCs and VOIs in neutralization
880 assays. **e** Schematics of the plaque-reduction neutralization tests (PRNTs) process (upper) and the
881 resulting IC_{50} values for B5-D3, Casirivimab, and hIgG1 against authentic SARS-CoV-2 (lower). **f,**
882 **g** Dose-response curves depicting the neutralization efficacy of B5-D3 (orange), Casirivimab
883 (purple), and hIgG1 (grey) in PRNTs against authentic SARS-CoV-2 Wuhan-Hu-1 and Delta strains
884 (**f**), and Omicron sub-lineages (**g**). Data are presented as mean ± standard deviation (SD) from
885 duplicate experiments.

886

887 **Fig. 2 Enhanced survival and reduced infection in K18-hACE2 mice through intranasal**
888 **prophylaxis with B5-D3 against SARS-CoV-2. a**–**e** Female K18-hACE2 mice, aged 10 to 12
889 months, were inoculated with 1×10^4 PFU of SARS-CoV-2 (Wuhan-Hu-1 strain). Mice were treated
890 with B5-D3 6 h prior (–6 h) via intranasal (IN, red) or intravenous (IV, green) routes, or 24 h post-
891 infection (+24 h, blue) via IV (n = 4 + 1). IN PBS administered 6 h prior to viral challenge served
892 as the vehicle control (black; n = 4 + 1), and PBS alone was used for mock control (grey; n = 3 + 1)
893 (**a**). Body weight and survival (n = 3 or 4) were monitored over 14 days (**b**, **c**). One mouse from
894 each group was sacrificed at 4 dpi for analysis of viral titers in lung homogenates using a median
895 tissue culture infectious dose ($TCID_{50}$) assay (**d**) and histological analysis of lung sections (upper,
896 IHC staining for N protein; lower, H&E staining) (**e**). Black arrows indicate alveolar thickening, and
897 yellow arrows show leukocyte infiltration. Scale bar = 100 μm. ND, not detected; LOD, limit of
898 detection. **f**–**i** Young female K18-hACE2 mice, aged 2 to 3 months, were inoculated similarly and
899 treated with B5-D3 via IN route at 24 h before (–24 h, pink), 6 h before (–6 h, red), or 24 h after
900 (+24 h, orange) the viral challenge (n = 5). Mice receiving IN PBS 6 h before infection served as

901 the vehicle control (black), with mock control mice receiving PBS alone (grey) (**f**). Body weight (**g**)
902 and survival (**h**) were recorded for 14 days. Neutralizing antibody titers against Wuhan-Hu-1 in
903 serum samples from surviving mice at 14 dpi were determined using Vero E6 cells (**i**). nAb,
904 neutralizing antibody. Data are presented as the geometric mean ± geometric SD. Statistical
905 significance was determined using Dunn's multiple comparisons test.
906
907 **Fig. 3 Efficient viral clearance at early stages through intranasal prophylaxis with B5-D3**
908 **against SARS-CoV-2 challenge in K18-hACE2 mice. a** Workflow diagram showing timelines and
909 treatments for different mouse groups. Young female K18-hACE2 mice aged 2 to 3 months received
910 prophylactic administration of PBS (black), B5-D3 (red), or B5-D3-LALA (purple) via the IN route
911 6 h prior to inoculation with 1×10^4 PFU of Wuhan-Hu-1. Mice inoculated with PBS instead of the
912 virus served as mock controls (grey). Mice from each treatment group were sacrificed for tissue
913 collection at 1, 2, and 4 dpi (n = 3 per time point). **b** Quantitative PCR results showing relative
914 amounts of *S* (upper) and *N* (lower) viral RNA in lung tissues collected from different groups at 1,
915 2, and 4 dpi, normalized to mouse *Gapdh*. **c** The titers of infectious viruses detected in lung
916 homogenates, measured by $TCID_{50}$ assays at 1, 2, and 4 dpi. **d, e** Fixed lung tissues were sectioned
917 and stained; IHC for viral N protein (**d**) and H&E staining for tissue damage (**e**) are shown (scale
918 bar = 100 μm). Data presented as mean ± standard error of the mean (SEM). Statistical significance
919 was determined by Tukey's multiple comparisons test.
920
921

922 **Fig. 4 Transcriptomic analysis of lungs revealed early immune activation in IN B5-D3-**
923 **prophylaxis mouse group after SARS-CoV-2 challenge. a–d** DGE analysis comparing PBS (**a**),
924 B5-D3 (**c**), and B5-D3-LALA (**d**) against the mock control at specific time points (n = 3). Volcano
925 plots illustrate the gene expression changes (**a**, **c**, **d**), while red and blue dots represent significantly
926 upregulated and downregulated genes, respectively, with $|\log_2$ fold change ($\log_2$FC)$| \geq 1$ and a false
927 discovery rate (FDR) < 0.05. Bar chart in **b** shows the enrichment of GOBP "response to virus"
928 observed in PBS groups at 1, 2, 4 dpi, in which adjusted p values are indicated for individual
929 comparisons. **e–g** Comparison between IN B5-D3 and PBS group at 1 dpi. Volcano plot illustrates
930 the DGE analysis between IN B5-D3 to PBS group at 1 dpi (**e**), with red and blue dots representing
931 significantly upregulated and downregulated genes, respectively, with $|\log_2\text{FC}| \geq 1$ and FDR < 0.05.
932 GSEA shows top 15 significantly activated GOBPs (**f**) and KEGG pathways (**g**) in IN B5-D3
933 compared to PBS group at 1 dpi. NES, normalized enrichment score; p.adj, adjusted p value. **h–j**
934 GSEA plots of chemotaxis (**h**), Rap1 signaling pathway (**i**), and Th1 and Th2 cell differentiation (**j**)
935 in B5-D3 vs PBS comparison at 1 dpi. **k**, **l** Heatmaps show NES of GSEA comparing various
936 treatments to the mock control (**k**) and between B5-D3 to PBS (**l**), focusing on top 10 GOBPs in **f**
937 and **Supplementary Fig. 10c, d**, respectively, and those related to immune cell chemotaxis.
938 Significant NES values ($p < 0.05$, FDR < 0.25) are highlighted in yellow. Purple boxes indicate
939 GOBPs where B5-D3 (1 dpi) group shows activation but PBS (1 dpi) group shows suppression.
940 Benjamin–Hochberg method was used for FDR adjustment.
941
942 **Fig. 5 *In vivo* bio-distribution of B5-D3 after IN administration. a** Schematic workflow of *in*
943 *vivo* and *ex vivo* imaging. Female K18-hACE2 mice aged 2 to 3 months received IN administration
944 of fluorescently labeled B5-D3 (B5-D3-AF750) and was visualized at different time points. **b**
945 Representative whole-body images of control and treated mice at 5 min, 1 h, and 24 h after B5-D3-

946 AF750 administration, showing the signal captured by *in vivo* imaging (left). White circles indicate
947 regions of interest (ROIs) for quantification of fluorescence signals in the nasal cavities. Average
948 (Avg) Radiance measured at all time points are shown on the right. **c** *Ex vivo* images of tissues from
949 control and treated mice sacrificed at indicated time points after B5-D3-AF750 administration. Blue
950 circles indicate ROIs for signal quantification. Br, brain; NC, nasal cavity; T, trachea; Lu, lung; H,
951 heart; Lv, liver; S, spleen; K, kidney; UB, urinary bladder; Bl, blood; Ur, urine. **d** Avg Radiance
952 shows the fluorescence signals in excised tissues measured *ex vivo*. **e** Schematic workflow for BALF
953 analysis. Female K18-hACE2 mice aged 2 to 3 months received IN administration of B5-D3-AF750
954 (n = 3) or PBS (n = 4) and were sacrificed at 6 h later for collection of BALF cells. **f** Percentage of
955 $CD45^+$ cells in live BALF cells. **g** Positive rates (left) and histograms (right) of B5-D3
956 binding/uptake in $CD45^+$ BALF cells. Histograms show B5-D3-AF750 fluorescence intensities in
957 $CD45^+$ BALF cells from individual mice. **h** Frequency of individual immune cell types in $CD45^+$B5-
958 $D3^+$ BALF cells. Red arrows point out AMs and mono-Macs with high abundance. AM, alveolar
959 macrophage; Mono-Mac, monocyte-derived macrophage; cDC1/2, type 1 or 2 conventional
960 dendritic cells. **i**, **j** Positive rates (left) and histograms (right) of B5-D3 binding/uptake in
961 $CD11c^+$Siglec-F^+ AMs (**i**) and $CD11b^-$F4/80^+ mono-Macs (**j**). **k** Median fluorescence intensity (MFI)
962 of AF750 indicates B5-D3 binding/uptake in different $CD45^+$B5-$D3^+$ populations. **l** Confocal
963 images (scale bar = 50 μm) of BALF cells collected at 6 h and stained for sACE2-Fc (red, anti-Fc,
964 Abcam #ab98596), Siglec-F (green, BD #564514), and nuclei (blue, Hoechst). Magnified views are
965 shown in white rectangles. Data are presented as mean ± SEM, and statistical significance was
966 determined by Tukey's multiple comparisons test or Student's t-test.

967

968 **Fig. 6 B5-D3 enhanced phagocytosis and degradation of SARS-CoV-2 pseudovirus in THP-1-**
969 **derived macrophages. a** Immunostaining of p24 (Invitrogen #PA5-81773), sACE2-Fc, and

970 LAMP1 (Abcam #ab25630) in THP-1-differentiated M0 macrophages showing phagocytosis of
971 SARS-CoV-2 pseudovirus (PV, $p24^+$) after 6 h of incubation with or without B5-D3 (scale bar = 50
972 μm). LAMP1 was stained to identify lysosomes. **b** Quantification of p24 signal intensity as shown
973 in **a**. Intensity Density (IntDen) per cell number indicates the mean p24 signal per cell, calculated
974 using ImageJ. Each dot represents one image. **c** Manders' coefficient indicating the colocalization
975 of p24 and LAMP1 in THP-1 M0 macrophages as shown in **a**. **d** Immunostaining of p24, sACE2-
976 Fc, and LAMP1 in hACE2-Calu-3 cells after 6 h incubation with pseudovirus, with or without B5-
977 D3 (scale bar = 50 μm). **e** Quantification of mean p24 signal intensity as shown in **d**. **f** Manders'
978 coefficient for the colocalization of p24 and LAMP1 in hACE2-Calu-3 cells, as shown in **d**. **g**
979 Quantification of pseudovirus infection in THP-1, M0 macrophages, M1 macrophages, hACE2-
980 Calu-3, and hACE2-293T cells, in the presence or absence of B5-D3. Results shown are luciferase
981 activities measured at 2 days post-transduction. **h** Immunoblot staining of cell lysates to detect
982 SARS-CoV-2 spike cleavage after cell entry. M0 macrophages, M1 macrophages, and hACE2-293T
983 cells were incubated with pseudovirus for 6 h, with or without B5-D3, before protein extraction.
984 Band locations of SARS-CoV-2 spike S2 and S2′ fragments are labeled in black and red respectively.
985 Data are presented as mean ± SEM, and statistical significance was determined by Tukey's multiple
986 comparisons test.

987

988 **Fig. 7 Proposed mechanisms of action of IN sACE2-Fc decoy in preventing SARS-CoV-2**
989 **infection. a, b** Schematics illustrating the actions and outcomes of SARS-CoV-2 infection, in the
990 absence (**a**) and presence (**b**) of IN delivered sACE2-Fc decoys. The figure was generated in
991 Biorender.

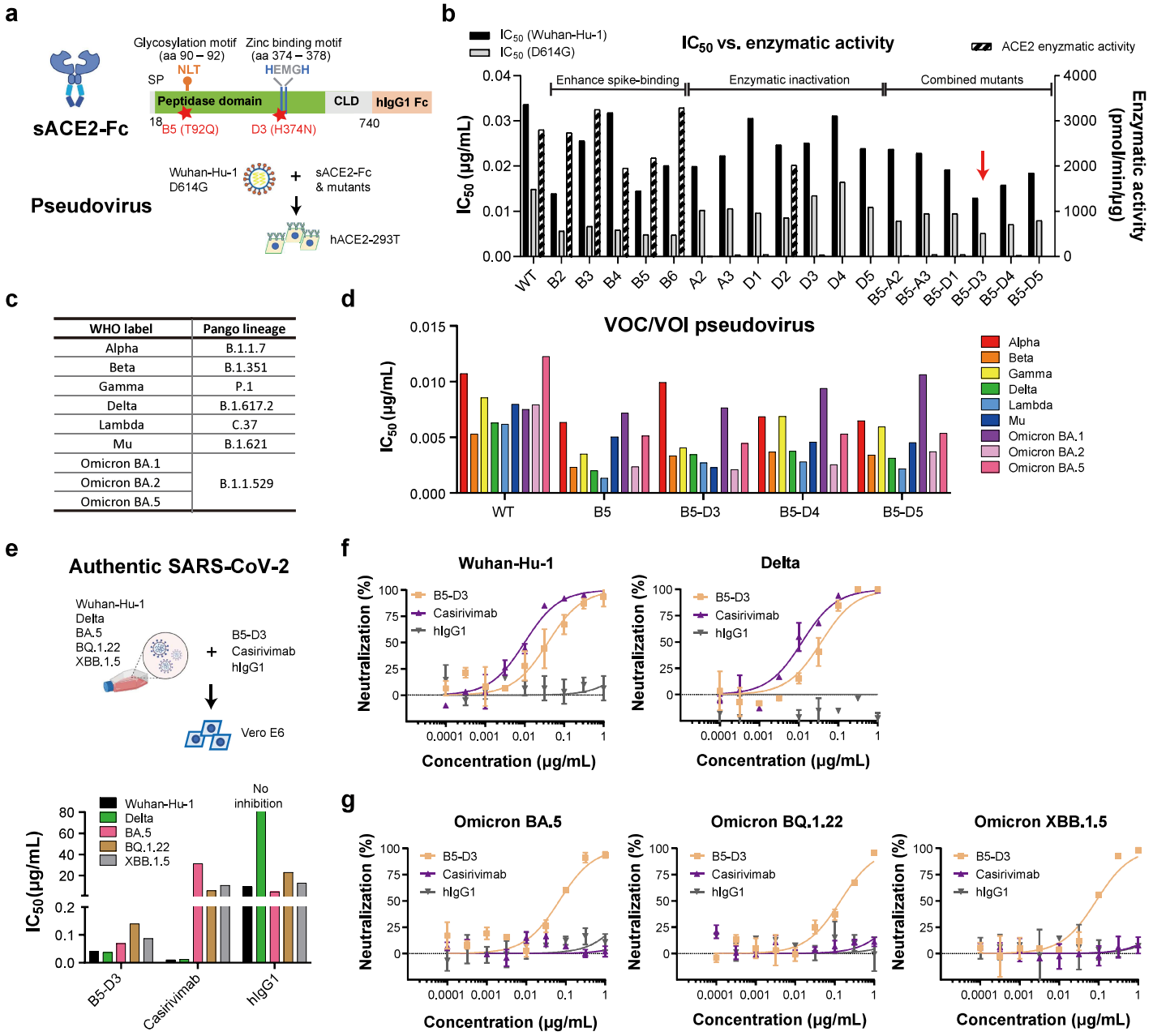

WHO label	Pango lineage
Alpha	B.1.1.7
Beta	B.1.351
Gamma	P.1
Delta	B.1.617.2
Lambda	C.37
Mu	B.1.621
Omicron BA.1	B.1.1.529
Omicron BA.2	
Omicron BA.5	

Figure 1

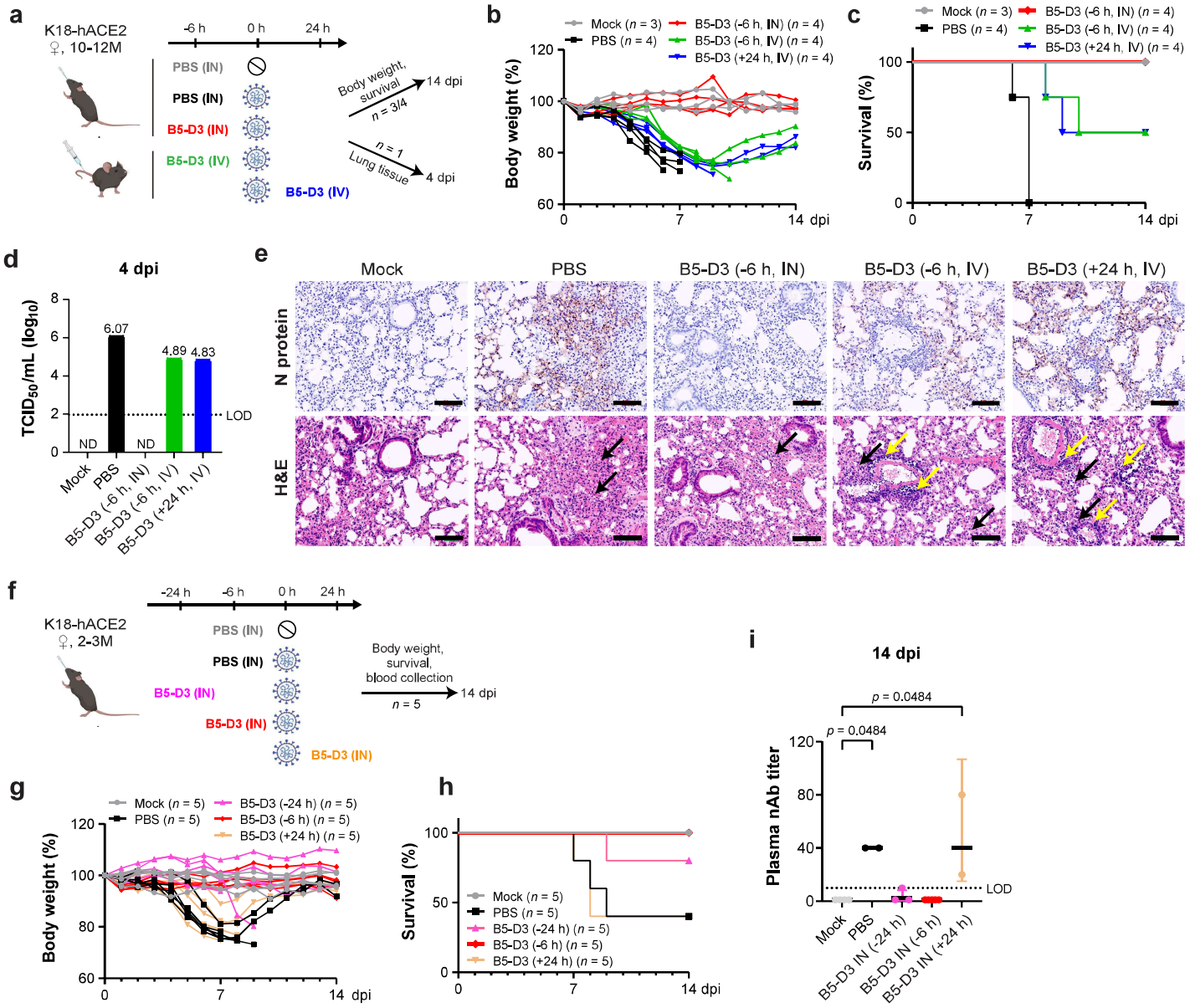
a
K18-hACE2
♀, 10-12M
-6 h
0 h
24 h
PBS (IN)
PBS (IN)
B5-D3 (IN)
B5-D3 (IV)
B5-D3 (IV)
Body weight, survival
n = 3/4
14 dpi
n = 1
Lung tissue
4 dpi
b
Mock (n = 3)
PBS (n = 4)
B5-D3 (-6 h, IN) (n = 4)
B5-D3 (-6 h, IV) (n = 4)
B5-D3 (+24 h, IV) (n = 4)
Body weight (%)
14 dpi
c
Survival (%)
14 dpi
d
4 dpi
TCID50/mL (log10)
6.07
4.89
4.83
ND
ND
LOD
Mock
PBS
B5-D3 (-6 h, IN)
B5-D3 (-6 h, IV)
B5-D3 (+24 h, IV)
e
Mock
PBS
B5-D3 (-6 h, IN)
B5-D3 (-6 h, IV)
B5-D3 (+24 h, IV)
N protein
H&E
f
K18-hACE2
♀, 2-3M
-24 h
-6 h
0 h
24 h
PBS (IN)
PBS (IN)
B5-D3 (IN)
B5-D3 (IN)
B5-D3 (IN)
Body weight, survival, blood collection
n = 5
14 dpi
g
Mock (n = 5)
PBS (n = 5)
B5-D3 (-24 h) (n = 5)
B5-D3 (-6 h) (n = 5)
B5-D3 (+24 h) (n = 5)
Body weight (%)
14 dpi
h
Survival (%)
Mock (n = 5)
PBS (n = 5)
B5-D3 (-24 h) (n = 5)
B5-D3 (-6 h) (n = 5)
B5-D3 (+24 h) (n = 5)
14 dpi
i
14 dpi
p = 0.0484
p = 0.0484
Plasma nAb titer
LOD
Mock
PBS
B5-D3 IN (-24 h)
B5-D3 IN (-6 h)
B5-D3 IN (+24 h)

Figure 2

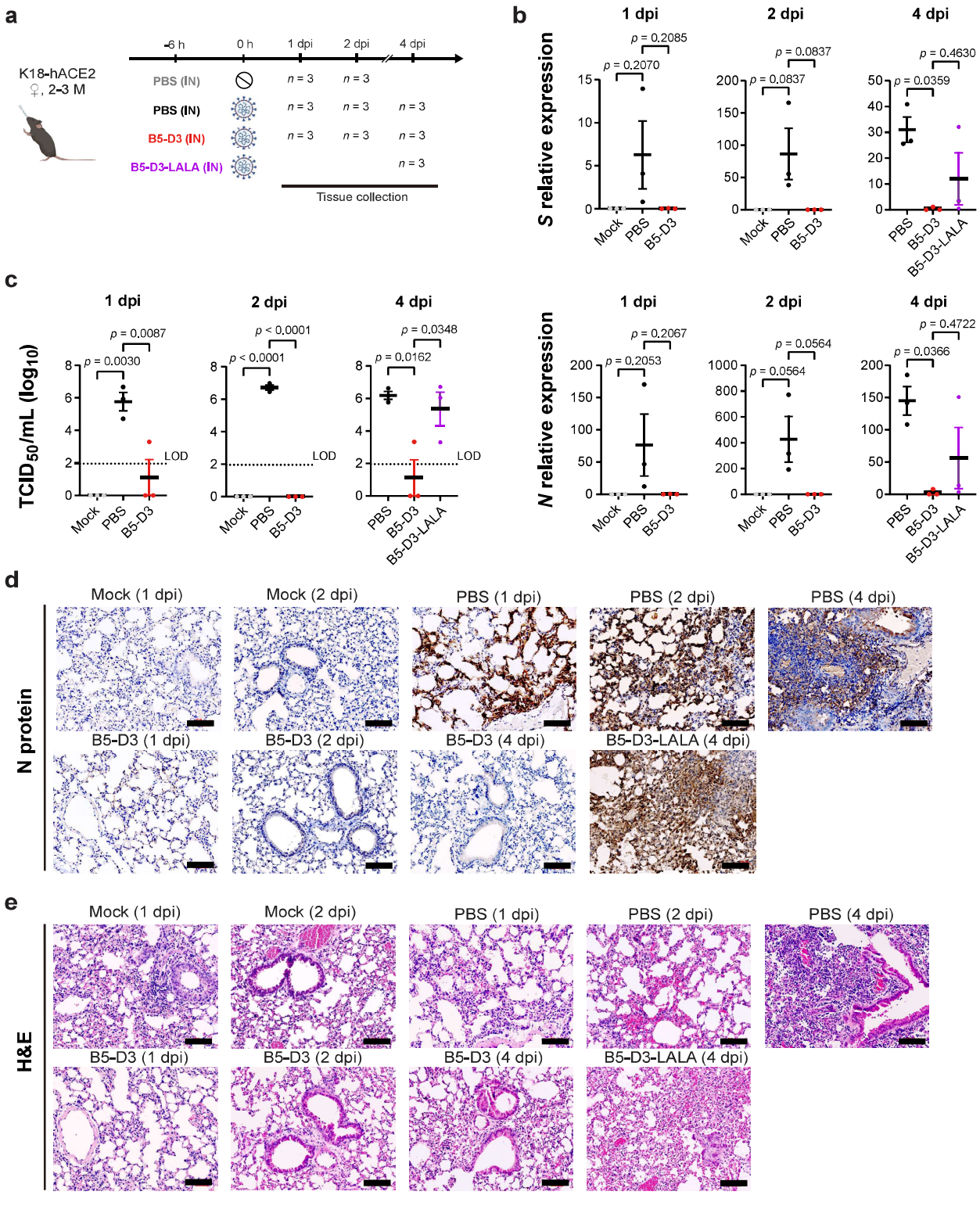
a
K18-hACE2
♀, 2-3 M
-6 h
0 h
1 dpi
2 dpi
4 dpi
PBS (IN)
n = 3
PBS (IN)
B5-D3 (IN)
B5-D3-LALA (IN)
Tissue collection
b
1 dpi
2 dpi
4 dpi
S relative expression
p = 0.2085
p = 0.2070
p = 0.0837
p = 0.0837
p = 0.4630
p = 0.0359
Mock
PBS
B5-D3
B5-D3-LALA
c
TCID50/mL (log10)
p = 0.0087
p = 0.0030
p < 0.0001
p < 0.0001
p = 0.0348
p = 0.0162
LOD
N relative expression
p = 0.2067
p = 0.2053
p = 0.0564
p = 0.0564
p = 0.4722
p = 0.0366
d
N protein
Mock (1 dpi)
Mock (2 dpi)
PBS (1 dpi)
PBS (2 dpi)
PBS (4 dpi)
B5-D3 (1 dpi)
B5-D3 (2 dpi)
B5-D3 (4 dpi)
B5-D3-LALA (4 dpi)
e
H&E
Mock (1 dpi)
Mock (2 dpi)
PBS (1 dpi)
PBS (2 dpi)
PBS (4 dpi)
B5-D3 (1 dpi)
B5-D3 (2 dpi)
B5-D3 (4 dpi)
B5-D3-LALA (4 dpi)

Figure 3

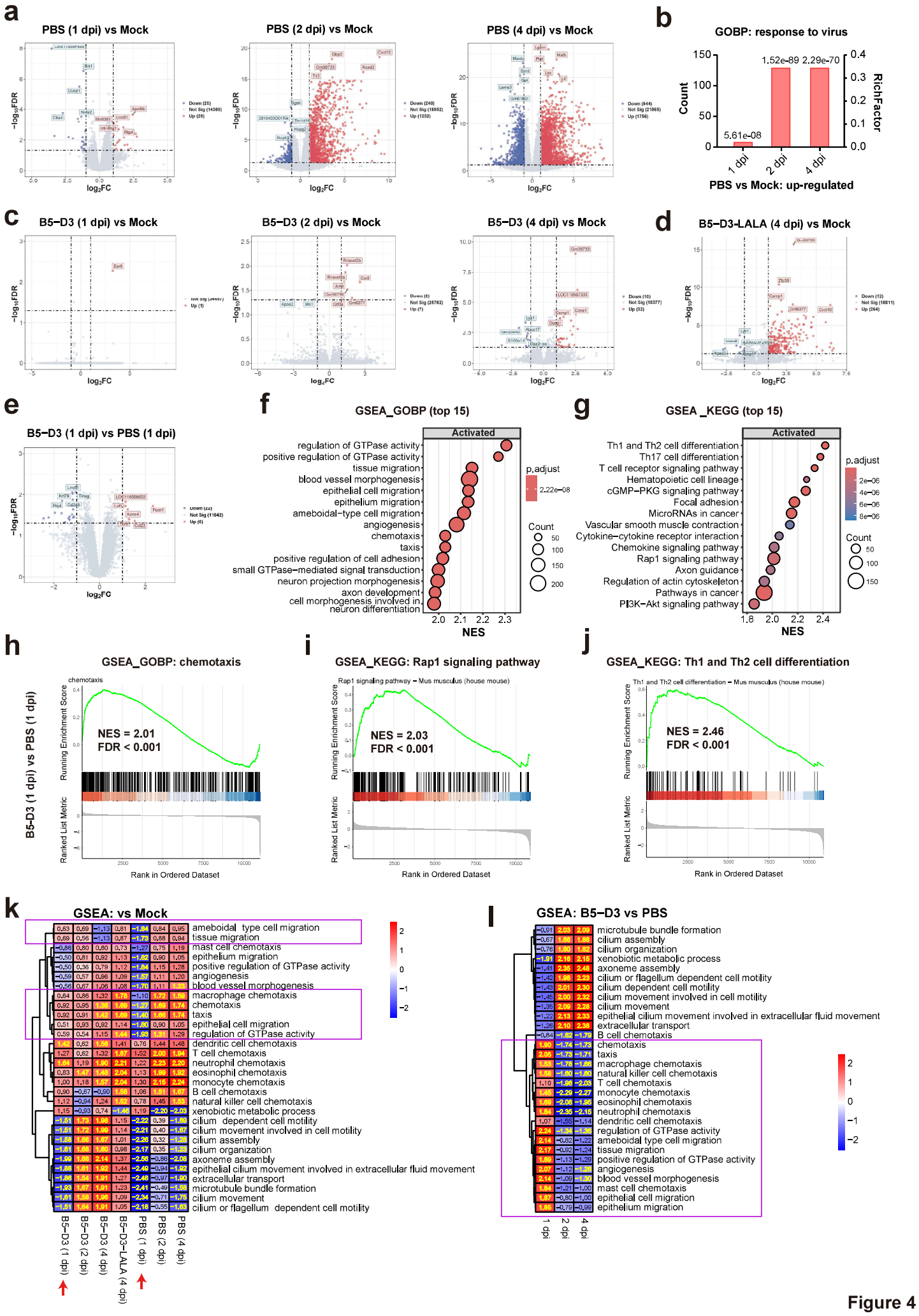
a
PBS (1 dpi) vs Mock
PBS (2 dpi) vs Mock
PBS (4 dpi) vs Mock
b
GOBP: response to virus
Count
RichFactor
1.52e-89
2.29e-70
5.61e-08
1 dpi
2 dpi
4 dpi
PBS vs Mock: up-regulated
c
B5−D3 (1 dpi) vs Mock
B5−D3 (2 dpi) vs Mock
B5−D3 (4 dpi) vs Mock
d
B5−D3-LALA (4 dpi) vs Mock
e
B5−D3 (1 dpi) vs PBS (1 dpi)
f
GSEA_GOBP (top 15)
Activated
regulation of GTPase activity
positive regulation of GTPase activity
tissue migration
blood vessel morphogenesis
epithelial cell migration
epithelium migration
ameboidal−type cell migration
angiogenesis
chemotaxis
taxis
positive regulation of cell adhesion
small GTPase−mediated signal transduction
neuron projection morphogenesis
axon development
cell morphogenesis involved in neuron differentiation
p.adjust
2.22e−08
Count
NES
g
GSEA _KEGG (top 15)
Activated
Th1 and Th2 cell differentiation
Th17 cell differentiation
T cell receptor signaling pathway
Hematopoietic cell lineage
cGMP−PKG signaling pathway
Focal adhesion
MicroRNAs in cancer
Vascular smooth muscle contraction
Cytokine−cytokine receptor interaction
Chemokine signaling pathway
Rap1 signaling pathway
Axon guidance
Regulation of actin cytoskeleton
Pathways in cancer
PI3K−Akt signaling pathway
p.adjust
Count
NES
h
GSEA_GOBP: chemotaxis
B5−D3 (1 dpi) vs PBS (1 dpi)
NES = 2.01
FDR < 0.001
Running Enrichment Score
Ranked List Metric
Rank in Ordered Dataset
i
GSEA_KEGG: Rap1 signaling pathway
NES = 2.03
FDR < 0.001
j
GSEA_KEGG: Th1 and Th2 cell differentiation
NES = 2.46
FDR < 0.001
k
GSEA: vs Mock
ameboidal type cell migration
tissue migration
mast cell chemotaxis
epithelium migration
positive regulation of GTPase activity
angiogenesis
blood vessel morphogenesis
macrophage chemotaxis
chemotaxis
taxis
epithelial cell migration
regulation of GTPase activity
dendritic cell chemotaxis
T cell chemotaxis
neutrophil chemotaxis
eosinophil chemotaxis
monocyte chemotaxis
B cell chemotaxis
natural killer cell chemotaxis
xenobiotic metabolic process
cilium dependent cell motility
cilium movement involved in cell motility
cilium assembly
cilium organization
axoneme assembly
epithelial cilium movement involved in extracellular fluid movement
extracellular transport
microtubule bundle formation
cilium movement
cilium or flagellum dependent cell motility
B5−D3 (1 dpi)
B5−D3 (2 dpi)
B5−D3 (4 dpi)
B5−D3−LALA (4 dpi)
PBS (1 dpi)
PBS (2 dpi)
PBS (4 dpi)
l
GSEA: B5−D3 vs PBS
microtubule bundle formation
cilium assembly
cilium organization
xenobiotic metabolic process
axoneme assembly
cilium or flagellum dependent cell motility
cilium dependent cell motility
cilium movement involved in cell motility
cilium movement
epithelial cilium movement involved in extracellular fluid movement
extracellular transport
B cell chemotaxis
chemotaxis
taxis
macrophage chemotaxis
natural killer cell chemotaxis
T cell chemotaxis
monocyte chemotaxis
eosinophil chemotaxis
neutrophil chemotaxis
dendritic cell chemotaxis
regulation of GTPase activity
ameboidal type cell migration
tissue migration
positive regulation of GTPase activity
angiogenesis
blood vessel morphogenesis
mast cell chemotaxis
epithelial cell migration
epithelium migration
1 dpi
2 dpi
4 dpi

Figure 4

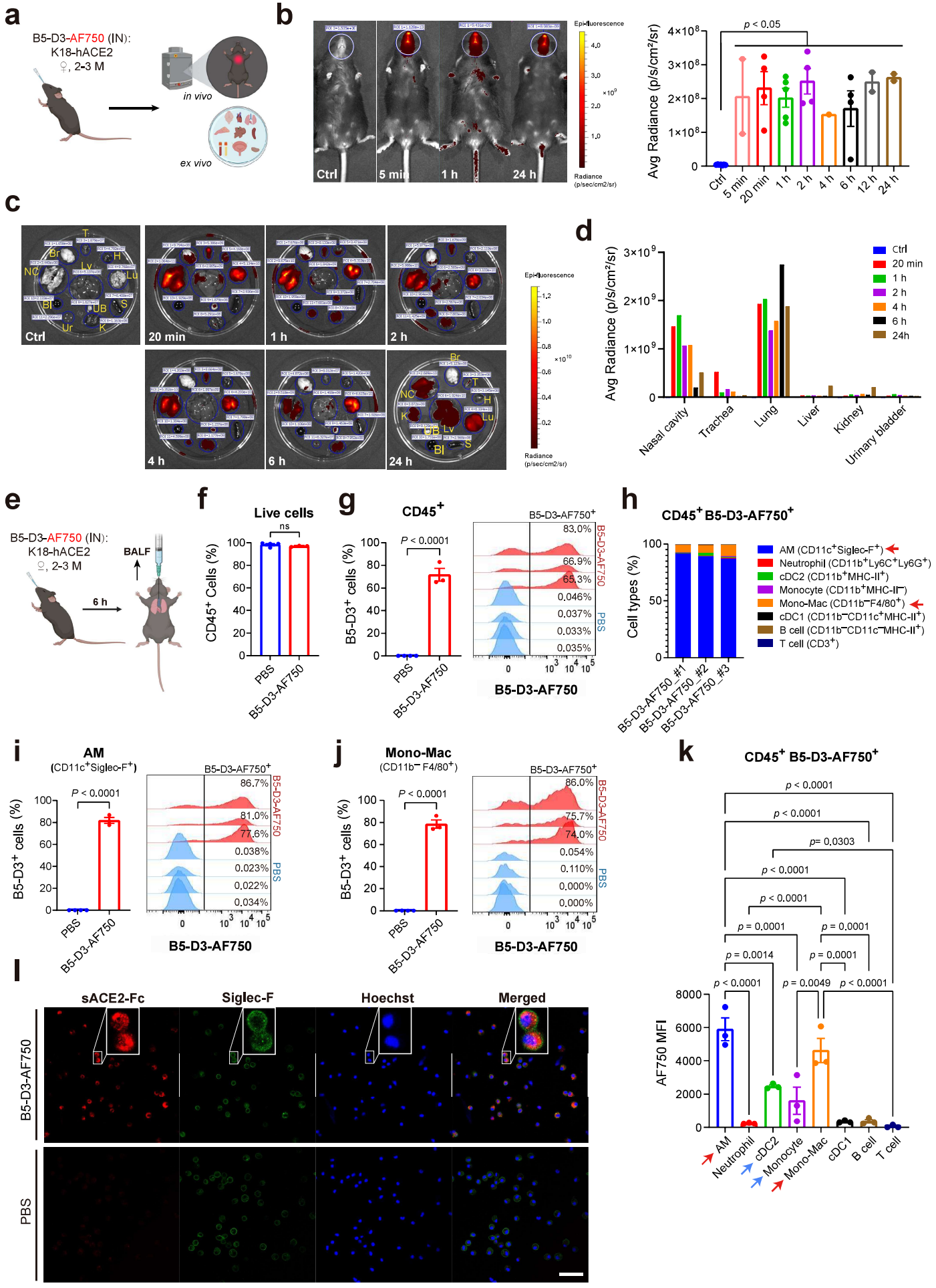
a
B5-D3-AF750 (IN):
K18-hACE2
♀, 2-3 M
in vivo
ex vivo
b
Ctrl
5 min
1 h
24 h
Epi-fluorescence
Radiance (p/sec/cm2/sr)
Avg Radiance (p/s/cm²/sr)
p < 0.05
Ctrl
5 min
20 min
1 h
2 h
4 h
6 h
12 h
24 h
c
Ctrl
20 min
1 h
2 h
4 h
6 h
24 h
Epi-fluorescence
Radiance (p/sec/cm2/sr)
d
Avg Radiance (p/s/cm²/sr)
Ctrl
20 min
1 h
2 h
4 h
6 h
24h
Nasal cavity
Trachea
Lung
Liver
Kidney
Urinary bladder
e
B5-D3-AF750 (IN):
K18-hACE2
♀, 2-3 M
6 h
BALF
f
Live cells
ns
CD45+ Cells (%)
PBS
B5-D3-AF750
g
CD45+
P < 0.0001
B5-D3+ cells (%)
B5-D3-AF750+
83.0%
66.9%
65.3%
0.046%
0.037%
0.033%
0.035%
B5-D3-AF750
PBS
B5-D3-AF750
h
CD45+ B5-D3-AF750+
Cell types (%)
AM (CD11c+Siglec-F+)
Neutrophil (CD11b+Ly6C+Ly6G+)
cDC2 (CD11b+MHC-II+)
Monocyte (CD11b+MHC-II−)
Mono-Mac (CD11b−F4/80+)
cDC1 (CD11b−CD11c+MHC-II+)
B cell (CD11b−CD11c−MHC-II+)
T cell (CD3+)
B5-D3-AF750_#1
B5-D3-AF750_#2
B5-D3-AF750_#3
i
AM
(CD11c+Siglec-F+)
P < 0.0001
B5-D3+ cells (%)
B5-D3-AF750+
86.7%
81.0%
77.6%
0.038%
0.023%
0.022%
0.034%
B5-D3-AF750
PBS
B5-D3-AF750
j
Mono-Mac
(CD11b− F4/80+)
P < 0.0001
B5-D3+ cells (%)
B5-D3-AF750+
86.0%
75.7%
74.0%
0.054%
0.110%
0.000%
0.000%
B5-D3-AF750
PBS
B5-D3-AF750
k
CD45+ B5-D3-AF750+
p < 0.0001
p < 0.0001
p= 0.0303
p < 0.0001
p < 0.0001
p = 0.0001
p = 0.0001
p = 0.0014
p = 0.0001
p < 0.0001
p = 0.0049
p < 0.0001
AF750 MFI
AM
Neutrophil
cDC2
Monocyte
Mono-Mac
cDC1
B cell
T cell
l
sACE2-Fc
Siglec-F
Hoechst
Merged
B5-D3-AF750
PBS

Figure 5

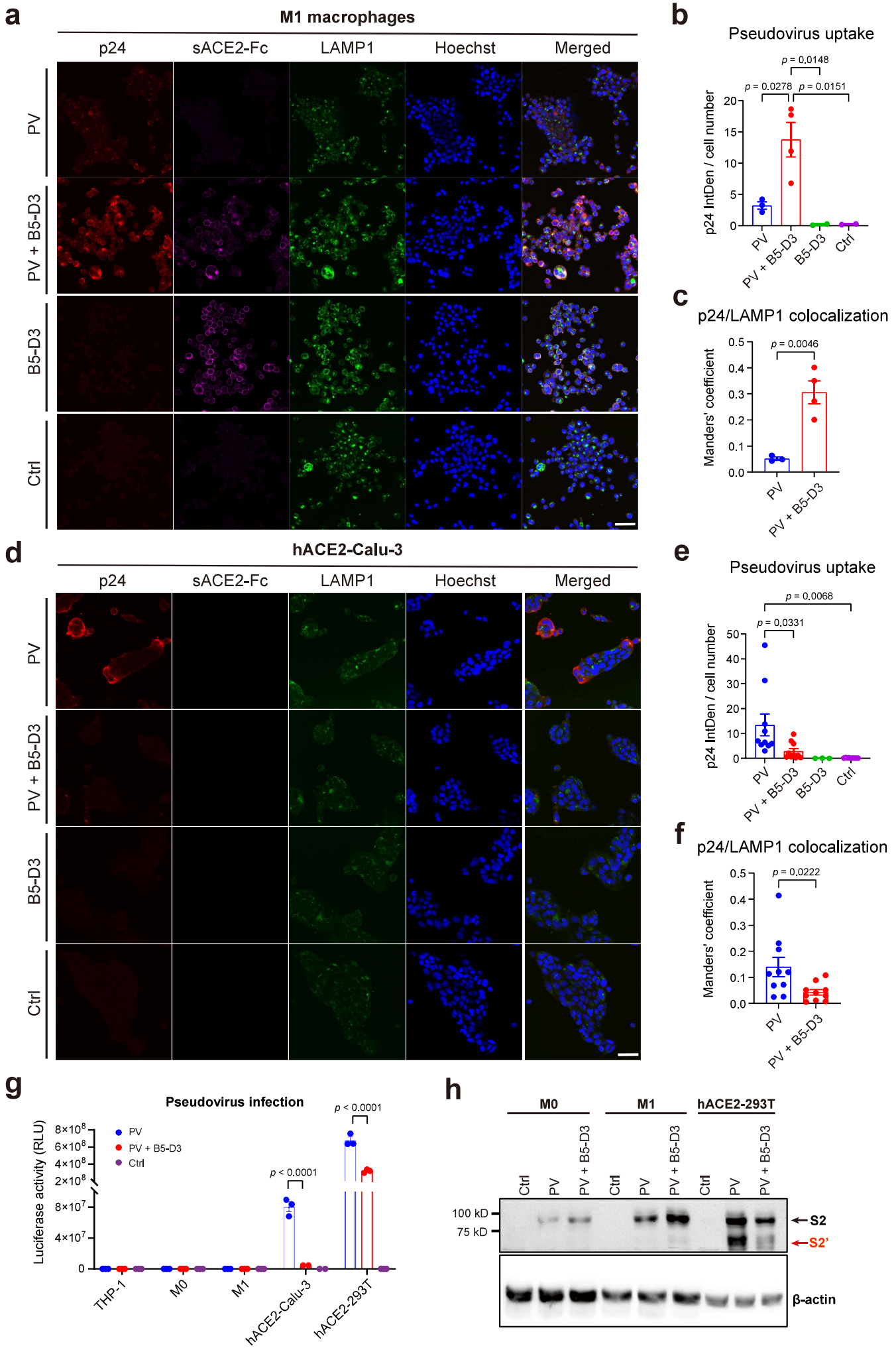
a
M1 macrophages
p24
sACE2-Fc
LAMP1
Hoechst
Merged
PV
PV + B5-D3
B5-D3
Ctrl
b
Pseudovirus uptake
p = 0.0148
p = 0.0278
p = 0.0151
p24 IntDen / cell number
PV
PV + B5-D3
B5-D3
Ctrl
c
p24/LAMP1 colocalization
p = 0.0046
Manders' coefficient
PV
PV + B5-D3
d
hACE2-Calu-3
p24
sACE2-Fc
LAMP1
Hoechst
Merged
PV
PV + B5-D3
B5-D3
Ctrl
e
Pseudovirus uptake
p = 0.0068
p = 0.0331
p24 IntDen / cell number
PV
PV + B5-D3
B5-D3
Ctrl
f
p24/LAMP1 colocalization
p = 0.0222
Manders' coefficient
PV
PV + B5-D3
g
Pseudovirus infection
PV
PV + B5-D3
Ctrl
p < 0.0001
p < 0.0001
Luciferase activity (RLU)
THP-1
M0
M1
hACE2-Calu-3
hACE2-293T
h
M0
M1
hACE2-293T
Ctrl
PV
PV + B5-D3
100 kD
75 kD
S2
S2'
β-actin

Figure 6

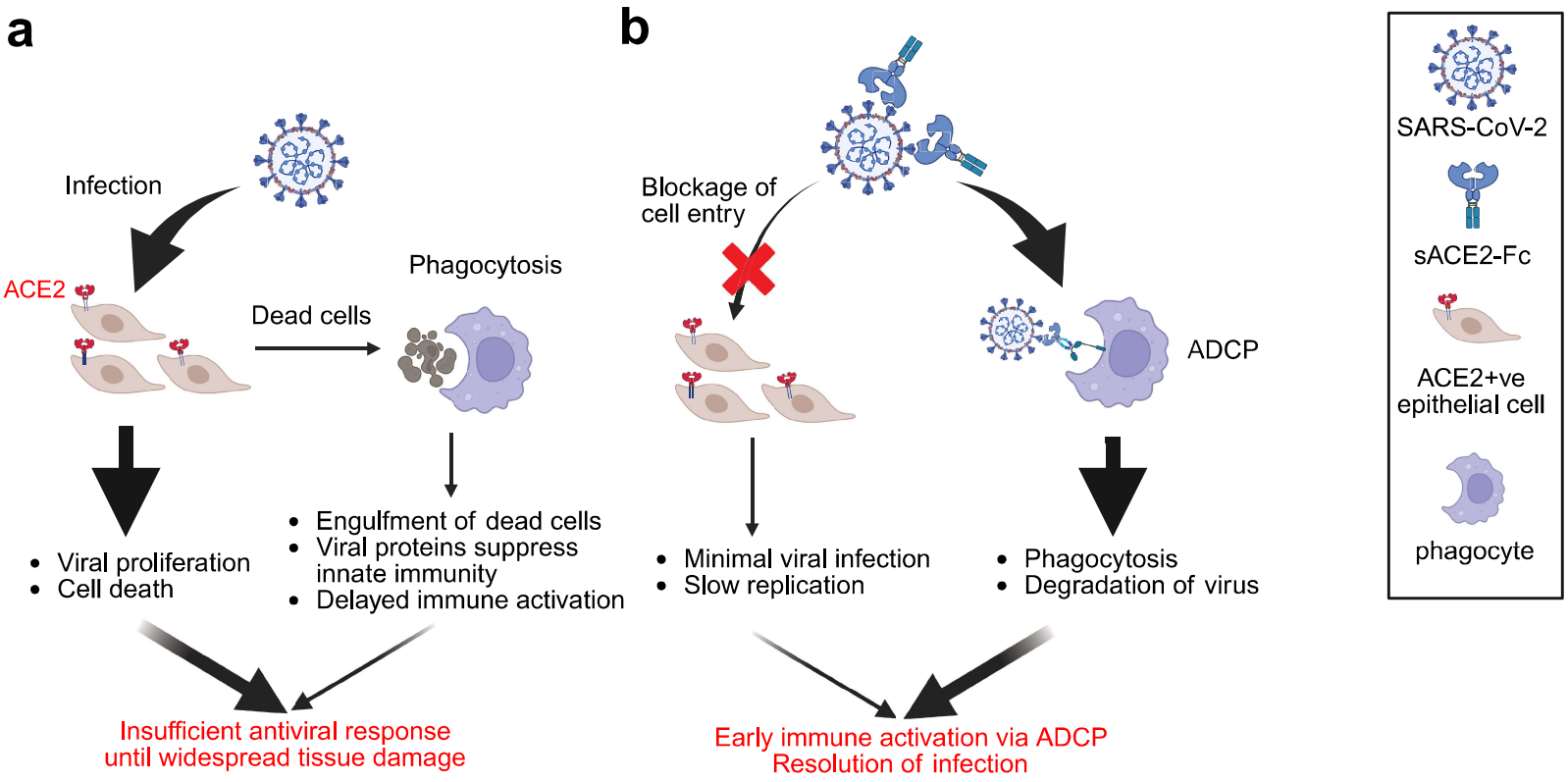
a
Infection
ACE2
Dead cells
Phagocytosis
Viral proliferation
Cell death
Engulfment of dead cells
Viral proteins suppress innate immunity
Delayed immune activation
Insufficient antiviral response until widespread tissue damage
b
Blockage of cell entry
ADCP
Minimal viral infection
Slow replication
Phagocytosis
Degradation of virus
Early immune activation via ADCP
Resolution of infection
SARS-CoV-2
sACE2-Fc
ACE2+ve epithelial cell
phagocyte

Figure 7